

GIST-PM-Asia v1: Development of a numerical system to improve particulate matter forecasts in South Korea using geostationary satellite-retrieved aerosol optical data over Northeast Asia

S. Lee¹, C. H. Song¹, R. S. Park^{1,5}, M. E. Park^{1,6}, K. M. Han¹, J. Kim², M. Choi², Y. S. Ghim³ and J.-H. Woo⁴

[1]{School of Environmental Science and Engineering, Gwangju Institute of Science and Technology (GIST), Gwangju, 500-712, Korea}

[2]{Department of Atmospheric Sciences, Yonsei University, Seoul, 120-749, Korea}

[3]{Department of Environmental Science, Hankuk University of Foreign Studies, Yongin, 449-791, Korea}

[4]{Department of Advanced Technology Fusion, Konkuk University, Seoul, 143-701, Korea}

[5]{Numerical Model Team, Korea Institute of Atmospheric Prediction Systems (KIAPS), Seoul, 156-849, Korea}

[6]{Asian Dust Research Division, National Institute of Meteorological Research (NIMR), Jeju-do, 697-845, Korea}

Correspondence to: C. H. Song (chsong@gist.ac.kr)

(For submission to **Geoscientific Model Development**)

Abstract

To improve short-term particulate matter (PM) forecasts in South Korea, the initial distribution of PM composition, particularly over the upwind regions, is primarily important. To prepare the initial PM composition, the aerosol optical depth (AOD) data retrieved from a geostationary equatorial orbit (GEO) satellite sensor, GOCI (Geostationary Ocean Color Imager) which covers Northeast Asia (113°E–146°E; 25°N–47°N), were used. Although GOCI can provide a higher number of AOD data in a semi-continuous manner than low Earth orbit (LEO) satellite sensors, it still has a serious limitation in that the AOD data are not available at cloud pixels and over high-reflectance areas, such as desert and snow-covered regions. To overcome this limitation, a spatio-temporal (ST) kriging method was used to better prepare the initial AOD distributions that were converted into the PM composition over Northeast Asia. One of the largest advantages in using the ST-kriging method in this study is that more observed AOD data can be used to prepare the best initial AOD fields compared with other methods that use single frame of observation data around the time of initialization. It is demonstrated in this study that the short-term PM forecast system developed with the application of the ST-kriging method can greatly improve PM₁₀ predictions in Seoul Metropolitan Area (SMA), when evaluated with ground-based observations. For example, errors and biases of PM₁₀ predictions decreased by ~60% and ~70%, respectively, during the first 6 h of short-term PM forecasting, compared with those without the initial PM composition. In addition, the influences of several factors on the performances of the short-term PM forecast were explored in this study. The influences of the choices of the control variables on the PM chemical composition were also investigated with the composition data measured via PILS-IC and low air-volume sample instruments at a site near Seoul. To

improve the overall performances of the short-term PM forecast system, several future research directions were also discussed and suggested.

Keywords: aerosol optical depth (AOD), short-term PM forecast, CMAQ model simulations, geostationary satellite, spatio-temporal kriging.

1 Introduction

It has been reported that there is a strong relationship between exposure to atmospheric particulate matter (PM) and human health (Brook et al., 2010; Brunekreef and Holgate, 2002; Pope and Dockery, 2006). PM has become a primary concern around the world, particularly in East Asia, where high PM pollution episodes have occurred frequently, mainly due to the large amounts of pollutant emissions from energetic economic activities. In an effort to understand the behaviors and characteristics of PM in East Asia, chemistry-transport models (CTMs) have played an important role in overcoming the spatial and temporal limitations of observations, and also enable policy makers to establish scientific implementation plans via making atmospheric regulations and policies. To improve the performance of the PM simulations, integrated air quality modeling systems that consist of CTMs, meteorological models, emissions, and data assimilation using ground- and satellite-borne measurements have been introduced (Al-Saadi et al., 2005; Park et al., 2011; Song et al., 2008). However, accurate simulations of PM distributions with CTMs have been challenging, because of many uncertainties from emission fluxes, meteorological fields, and chemical and physical parameterizations in the CTMs. For example, the Korean Ministry of Environment (MoE) has recently started to implement air quality forecasts for PM₁₀ over the Seoul metropolitan area (SMA), the largest metropolitan area in South Korea, and also plans to perform PM_{2.5} and ozone forecasts in 2015. However, the forecasting accuracy for high PM₁₀ alert (81 to 120 µg

69 m^{-3}) in the current system has been low (< 60%) since 2013. Thus, urgent improvements in
70 the PM_{10} predictions are necessary.

71 In this context, an improved short-term PM forecast system was developed and introduced,
72 based on an analogy to the system of numerical weather prediction (NWP). Figure 1(a)
73 presents a flow diagram of an NWP in which regional meteorological modeling is conducted
74 using two important inputs: (i) boundary conditions (BCs) from global meteorological models
75 and (ii) initial conditions (ICs) prepared via data assimilation using ground-measured data and
76 balloon-, ship-, aircraft-, and/or satellite-borne measurements. In contrast, conventional
77 chemical weather forecast (CWF) (e.g., forecasts for ozone and PM) has been carried out only
78 using meteorological fields and pollutant emissions (Fig. 1(b)). In the short-term PM forecast
79 system proposed here (Fig. 1(c)), one more input is added to the conventional CWF system:
80 the initial distribution of PM composition. To prepare the initial PM composition, a scheme
81 that uses geostationary satellite-derived aerosol optical depths (AODs), is developed in this
82 study. Similarly, the BCs for the CTM runs are obtained from global CTM simulations.

83 In the improved CWF system, AOD data retrieved from low Earth orbit (LEO) satellite
84 sensors, such as Moderate Resolution Imaging Spectroradiometer (MODIS) and Multi-angle
85 Imaging SpectroRadiometer (MISR) can be used to set up the ICs for the short-term PM
86 forecast (Benedetti et al., 2009; Liu et al., 2011; Saide et al., 2013). While these AOD data
87 have an advantage in spatial coverage compared with those obtained from point stations, the
88 use of the LEO satellite-derived AODs has another limitation in acquiring continuous
89 observations over a certain area due to the capabilities of the LEO sensors in their orbital
90 periods and viewing swath widths.

91 Such limitations in using LEO satellite observations can be overcome with the help of
92 geostationary (GEO) satellite sensors providing semi-continuous observations over a specific

part of the Earth during the day (Fishman et al., 2012; Lahoz et al., 2011; Zoogman et al., 2014). Recently, aerosol optical properties (AOPs) from the Geostationary Ocean Color Imager (GOCI) have become available. GOCI is the first multi-spectral ocean color sensor onboard the Communication, Ocean, and Meteorological Satellite (COMS), launched over Northeast Asia in 2010, providing semi-continuous AOD, single scattering albedo (SSA), and fine mode fraction (FMF) over a domain of Northeast Asia (Lee et al., 2010). With GOCI AOD data, a novel approach was developed to investigate transboundary PM pollution over Northeast Asia (Park et al., 2014a).

In this study, we carried out hindcast studies (forecast studies with past data) to find the “best” method to improve the performance of the short-term PM forecasting using the GOCI AODs. To do this, we developed a model, *Geostatistical Interpolation of Spatio-Temporal data for PM forecasting over Northeast Asia (GIST-PM-Asia) v1* that includes: (i) a spatio-temporal kriging (ST-kriging) method to spatio-temporally combine the GOCI-derived AODs, (ii) “observation operators” to convert the CTM-simulated PM composition into AODs and vice versa, and (iii) selection of “control variables” (CVs) through which the distribution of AODs can be converted back into the distributions of the PM composition to be used as the ICs. The uses of the ST-kriging method, observation operators, and CVs are illustrated in Fig. 1. The main advantages of using the ST-kriging method are discussed in detail in the main text. Several sensitivity studies were also conducted to improve the understanding of forecasting errors and biases in the short-term PM forecasting system developed.

With these research objectives and methodology, this paper is organized as follows: the hindcast framework is first described in detail in Sect. 2. In Sect. 3, the hindcast results with various configurations are evaluated with ground-based observations during the high PM

episodes in SMA to find the “best” configuration for future short-term PM forecast. After that, a summary and conclusions are provided in Sect. 4.

2 Methodology

With AOD data from both the GOCI sensor and CTM model simulations, the initial aerosol composition was prepared. For the CTM simulations, the Community Multi-scale Air Quality (CMAQ; ver. 5.0.1) model (Byun and Ching, 1999; Byun and Schere, 2006) together with the Weather Research and Forecast (WRF; ver. 3.5.1) (Skamarock and Klemp, 2008) were used. The ST-kriging method and 12 different combinations of observation operators and CVs were also used for preparing the distributions of the 3-D PM composition over the GOCI-covered domain. The CMAQ model simulations with the 12 different configurations were carried out and the performances were then tested against ground-measured AOD, PM₁₀, and PM_{2.5} composition. The details of these components are described in the following sections.

2.1 Meteorological and chemistry-transport modeling

The WRF model provided meteorological data with 15 km × 15 km horizontal grid spacing and 26 vertical layers extending up to 50 hPa. To obtain highly-resolved terrestrial input data, the topography height from NASA Shuttle Radar Topography Mission (SRTM) 3 arc-second database (http://dds.cr.usgs.gov/srtm/version2_1/SRTM3) and the land use information provided by Environmental Geographic Information Service (EGIS; <http://egis.me.go.kr>) were used. Initial and boundary meteorological conditions for the WRF simulation were provided by the National Centers for Environmental Protection (NCEP) final operational global tropospheric analyses (<http://rda.ucar.edu/datasets/ds083.2>). To improve 3-D temperature, winds and water vapor mixing, objective analysis was employed by

incorporating the NCEP ADP Global surface and upper air observation data. The meteorological fields were provided with 1-h temporal resolution, and were then converted into the input fields for the CMAQ model simulations by the Meteorology-Chemistry Interface Processor (MCIP; ver. 4.1) (Otte and Pleim, 2010).

The CMAQ model is a chemistry-transport model that simulates the chemical fates and transport of gaseous and particulate pollutants. In this study, the CMAQ modeling covered Northeast Asia, from 92° to 149° E and 17° to 48° N, using 15 km × 15 km horizontal grid spacing (Fig. 2) with 14 terrain following σ -coordinates, from 1000 to 94 hPa. The configurations of the WRF model and CMAQ simulation used in this study are described in Table 1.

Anthropogenic emission inputs were processed by Sparse Matrix Operator Kernel Emissions in Asia (SMOKE-Asia; ver. 1.2.1), which has been developed for processing anthropogenic emissions for Asia. Details of SMOKE-Asia were described in Woo et al. (2012). Biogenic emissions were prepared using the Model of Emission of Gases and Aerosol from Nature (MEGAN; ver. 2.0.4) (Guenther et al., 2006) with the MODIS-derived leaf area index (Myneni et al., 2002), MODIS land-cover data sets (Friedl et al., 2002), and the meteorological input data described above. For the consideration of biomass burning emissions, daily fire estimates provided by Fire Inventory from NCAR (FINN) were used (Wiedinmyer et al., 2011). Asian mineral dust emissions were not considered in this study. Thus, the periods for model evaluation were selected during periods when mineral dust events did not take place.

To take full advantage of the AOD data sets intensively measured during the Distributed Regional Aerosol Gridded Observation Network in Asia (DRAGON-Asia) campaign, modeling episodes were chosen for the campaign period from 1 March to 31 May 2012. First, background CMAQ model simulations were conducted for the 3-month DRAGON period

with 10-day spin-up modeling. After this, initial conditions were prepared using the ST-kriging method, observation operators and CVs via the combination of GOCI AODs with the background modeling AOD. Analysis was carried out for 12-h from 12:00 in local time (LT) on 10 selected high PM pollution days. Each hindcast hour is referred to be H+0 to H+12. In this study we paid more attention to the performance of the first 12-h PM₁₀ hindcast results, and the analysis of the hindcast results after 13 h is also discussed briefly in Sect. 3.3.

In the hindcast analysis, different hindcast runs with 12 combinations of different observation operators and CVs were conducted, as discussed in Sect. 2.4 and 2.5. We selected 1 episode from March (28 March), 5 episodes from April (8, 9, 14, 17, and 23 April), and 4 episodes from May (6, 13, 15, and 16 May), 2012 for the analysis associated with three criteria of: (i) on the selected days the average PM₁₀ from 12:00 to 18:00 LT was above 70 $\mu\text{g m}^{-3}$ over SMA, (ii) on the selected days, the daily coverage of the GOCI AOD data was at least 20 % over the GOCI domain, and (iii) on the selected days, dust events were not recorded over South Korea according to the Korea Meteorological Administration (KMA). Additional hindcast runs were also conducted from 7 March 12:00 to 19 March 11:00 for evaluating the performances of the hindcast runs for less polluted episodes. In this study, we focused on SMA, because we were particularly interested in this area. However, the system introduced here can be applied to other areas inside the GOCI domain where surface PM observation data are available.

2.2 Observation data

2.2.1 GOCI AOD

As mentioned previously, GEO satellite sensors have important advantages compared with LEO satellite sensors, such as semi-continuously (with 1-h intervals) producing AOP data

186 over a specific domain of interest. Despite this temporal advantage, it has been difficult for
187 most GEO satellite sensors to produce accurate AOPs, because they have only one or two
188 visible channels. In contrast, the GOCI instrument has six visible and two near-infrared
189 channels, and can produce multi-spectral images eight times per day with a spatial resolution
190 of approximately $500\text{ m} \times 500\text{ m}$ with coverage of $2,500\text{ km} \times 2,500\text{ km}$, including part of
191 Northeast China, the Korean peninsula, and Japan (Fig. 2). Using the 1-h resolved multi-
192 spectral radiance data from GOCI, the uncertainties of AOP retrievals can be dramatically
193 reduced (Park et al., 2014a). The GOCI AOPs were retrieved with multi-channel algorithms
194 that can provide hourly AOP data including AOD, FMF, and SSA at 550 nm (Choi et al.,
195 2015). Compared with the algorithms from two previous studies (Lee et al., 2010, 2012), the
196 GloA2 algorithm uses an improved lookup table for retrieving the AOPs, using extensive
197 observations from Aerosol Robotic Network (AERONET) and monthly surface reflectance
198 observed from GOCI, and provides 1-h resolved AOP data at eight fixed times per day (from
199 09:30 to 16:30 LT) with $6\text{ km} \times 6\text{ km}$ spatial resolution. In this study, the AOD data from the
200 GOCI AOPs were used (because the SSA and FMF data need further improvements) and also
201 compared with collection-6 3 km MODIS aerosol products from the Aqua and Terra satellites
202 (Munchak et al., 2013) to present the relative performances of GOCI AOD. The AERONET
203 AOD data were also used for assessing the relative accuracy of the GOCI AODs. Figures 3(a)
204 and 3(b) show the scatter plot analyses of three satellite-retrieved AODs from Aqua MODIS,
205 Terra MODIS and GOCI vs. AERONET level 2 AODs over the GOCI domain during the
206 DRAGON-Asia campaign. All the satellite data were sampled within spatial and temporal
207 differences of 3 km and 10 min from the AERONET observations. It should also be noted that
208 the GOCI and MODIS data were compared with the AERONET data without the applications
209 of kriging method. First, it was found that GOCI provided more frequent AOD data ($N =$

2276) than MODIS ($N = 629$) and that GOCI AODs data show comparable regression coefficient ($R = 0.85$), root mean square error ($RMSE = 0.25$), and mean bias ($MB = -0.19$), compared with MODIS data ($R = 0.89$; $RMSE = 0.16$; $MB = 0.06$). This indicates that the GOCI AOD data not only have comparable quality to the MODIS AOD data, but also provide a higher number of data over the GOCI domain. In Fig. 3(c), the daily spatial AOD percent coverages of the Aqua/Terra MODIS and GOCI sensors are compared. It was found that there are a large number of daily missing pixels in the observations of both satellite sensors (the average percent coverages of Aqua MODIS, Terra MODIS and GOCI AODs during the period were about 9%, 10%, and 29%, respectively).

2.2.2 Ground-based observations

AERONET is a global ground-based sunphotometer network managed by the NASA Goddard Space Flight Center, providing spectral AOPs including AOD, SSA, and particle size distributions, available at <http://aeronet.gsfc.nasa.gov> (Holben et al., 1998). To match the wavelength of GOCI AOD with AERONET AOD, the AOD data at 550 nm were calculated via interpolation, using AODs and Ångström exponent data between 440 and 870 nm from the DRAGON-Asia level 2.0 data. AOD data from 29 AERONET sites inside the GOCI domain were used for validating GOCI and ST-kriging AOD products, and those from six AERONET sites in SMA were selected for evaluating the performance of hindcast AODs.

To analyze hindcast surface aerosol concentrations, the PM_{10} observations provided by the National Ambient Air Monitoring System (NAMIS) network in South Korea were used. The NAMIS network, operated by the MoE has collected air pollutant concentrations of PM_{10} measured by an automatic β -ray absorption method with a detection limit of $2 \mu g m^{-3}$ at 5-min

intervals. We selected 58 NAMIS sites in SMA, the locations of which are shown in Fig. 2, and used 1-h averaged data for the analysis during the selected episodes.

Ion concentrations of $\text{PM}_{2.5}$ were also measured using a particle-into-liquid sampler coupled with ion chromatography (PILS-IC) and a low air-volume sampler with a Teflon filter in Yongin City, located downwind of Seoul (Fig. 2). Details on the measurement methods are described in Lee et al. (2015) and are not repeated here. One-hour averaged sulfate (SO_4^{2-}), nitrate (NO_3^-), and ammonium (NH_4^+) concentrations, measured by the PILS-IC, and 24-h averaged SO_4^{2-} , NO_3^- , NH_4^+ , organic carbon (OC), and elementary carbon (EC), measured by the low air-volume sampler, were used for further comparison during the selected episodes (Sect. 3.4). The observed OC concentrations were multiplied by a factor of 1.5, to estimate organic aerosols (OAs) concentrations (He et al., 2011; Huang et al., 2010).

2.3 Spatio-temporal kriging

Kriging is a geostatistical interpolation method to estimate unmeasured variables and their uncertainties, using correlation structure of measured variables. An atmospheric application study of the kriging method to estimating PM_{10} exceedance days over Europe reported that ST-kriging showed comparable performances to those of the EnKF approach (Denby et al., 2008).

In this study, the ST-kriging method was used to fill out the missing pixels (Fig. 3(c)) with the spatial and temporal GOCI AOD data. The AOD fields produced by ST-kriging can be prepared with a horizontal resolution of $15 \text{ km} \times 15 \text{ km}$ from 10:00 LT to 16:00 LT over the GOCI domain. In this study, the AOD data at 12:00 LT (H+0) during the selected episode days were used for preparing the initial conditions. The details and general application of the

ST-kriging method are presented in Appendix A. One advantage of using ST-kriging in this study framework is to use large numbers of observational data (GOCI AODs), compared with other methods. In fact, the GOCI AOD data are densely available temporally (with 1-h intervals) and spatially (compared with MODIS AODs; see Figs. 3(a) and 3(b)). This was the primary reason for using the ST-kriging method in this study. For example, when initial AOD fields were prepared at a certain time (e.g., at noon, 12:00 LT: H+0), the ST-kriging method uses not only GOCI AOD data at 11:30 LT or 12:30 LT, but also GOCI AOD data at 09:30, 10:30, and 13:30, unlike other methods. In the case of 4 April, 2012 (a high PM pollution episode during the DRAGON-Asia campaign), other interpolation methods (e.g., Cressman, bilinear, and nearest-neighbor methods) could use only the GOCI AOD data of ~88,000 for the preparation of the initial AOD field at 12:00 LT, whereas the ST-kriging method used the GOCI AOD data of ~280,000 (3 times more AOD data). Sequential data assimilation (DA) methods such as OI and 3-DVAR can use the same number of observations as the ST-kriging method. However, they required four-step data assimilations (i.e. 4-hour time window for DA) to include observations from 09:30 to 13:30, thus greatly increasing the computational cost for daily assimilation.

If the observation data are densely available and the differences between the observations and model-simulated data are large (i.e., the model simulations include relatively large errors and biases), there is less “practical need” to use the CTM-simulated data in the process of data assimilation. That is, it would be more desirable if the values of the unobserved (missing) pixels could be filled in based on “more reliable” observation data (here, GOCI AODs). This would be particularly true, when the CTM-predicted AODs are systematically underestimated compared with GOCI or AERONET AODs (as will be shown in Fig. 5(a)). Additionally, computation costs of the ST-kriging method are so low that the ST-kriging AOD can be

calculated rapidly. For example, the 1-day process for preparing the AOD fields over the GOCI domain takes only ~20 min with two 3.47 GHz Xeon X5690 6-core processors and 32 gigabytes memory in the current application of the ST-kriging method. Thus, it can be applied directly to the daily CWF due to the relatively cheap computation cost. Again, computation time (rapid calculation) is a central issue in daily (short-term) chemical weather forecasts. The calculation of daily three-dimensional semivariogram takes most of the computation time (regarding the details of calculation of the daily three-dimensional semivariogram, refer to Appendix A and Fig. A1).

Connected with these discussions, in the application of the ST-kriging method to the GOCI AODs, the “optimal number” of observation data is necessary to balance the accuracy of the data and the computational speed. From many sensitivity tests (not shown here), the optimal number of observations for one white (missing) pixel is approximately 100. That is, the use of more observation data above this optimum number does not meaningfully enhance the accuracy of AODs of the missing pixels, but simply takes more computation time. This number of observation data is usually available for the most of the missing (white) pixels of the GOCI scenes from nearby grids both/either at the concurrent scene spatially within ~100 km and/or at the temporally-close snapshots within 3-h. Based on these reasons, the ST-kriging method was chosen for this study.

2.4 Observation operator

An observation operator (or forward operator) describes the relation between observation data and model parameters. For example, the observation operator in this study converts the aerosol composition into AODs (and vice versa). Based on the aerosol composition and the

relative humidity (RH) from the model simulations, simulated AODs at a wavelength of 550 nm (τ_{CMAQ}) were calculated with the following observation operator:

$$\tau_{CMAQ} = \sum_{s=1}^N \sum_{l=1}^M \alpha_{s,dry} f_s(RH_l) [C]_{s,l} H_l \quad (1)$$

where N and M denote the number of aerosol species (s) and model layer (l), respectively, $\alpha_{s,dry}$ the mass extinction efficiency (MEE) of the species, (s) at 550 nm under the dry condition, $f_s(RH_l)$ the hygroscopic enhancement factor for the species, (s) as a function of RH at the layer of l , $[C]_{s,l}$ the mass concentration of the species, (s) at the layer of l , and H_l the height of layer l . Here, $[C]_{s,l}$ is selected as the control variable (refer to Sect. 2.5).

In this study, three observation operators were used for calculating AODs and updating initial PM composition for the hindcast studies. The differences in the observation operators are caused mainly by the differences in $\alpha_{s,dry}$ and $f_s(RH_l)$ of Eq. (1). The first observation operator was selected from Goddard Chemistry Aerosol Radiation and Transport (GOCART) model (Chin et al., 2002; hereafter GOCART operator). Hygroscopic growth rates for SO_4^{2-} , OC, BC, and sea-salt aerosols were considered separately in this operator. The second observation operator was from the GEOS-Chem model (the GEOS-Chem operator). The detailed aerosol speciation and MEE values were described in Martin et al. (2003). Final observation operator is based on the study of Malm and Hand (2007) (the IMPROVE operator). This observation operator was based on the reconstruction method with the MEEs and hygroscopic enhancement factors at 550 nm for different types of aerosol species. Table 2 summarizes the characteristics of the three observation operators chosen in this study. To consistently consider the characteristics of the three observation operators, aerosol types (s in Eq. (1)) were classified into seven groups: SO_4^{2-} , NO_3^- , NH_4^+ , OAs, BC, sea-salt, and others, which mainly consist of $PM_{2.5}$ trace elements (Reff et al., 2009). In the classification, internal mixing

states of SO_4^{2-} , NO_3^- , and NH_4^+ were assumed. It should also be noted that the consideration of NO_3^- is important to correctly estimate AOD and aerosol mass loading in East Asia (Park et al., 2011, 2014b; Song et al., 2008). Figure 4 shows the **wet** MEE values ($\alpha_{s,wet}$, product of $\alpha_{s,dry}$ and $f_s(\text{RH}_l)$ in Eq. (1)) calculated for SO_4^{2-} , NO_3^- , and NH_4^+ at a wavelength of 550 nm as a function of RH, indicating that the three different operators can create large differences in the **wet** MEE values.

2.5 Selection of control variables

To prepare the distributions of the aerosol composition, the ST-kriging AOD fields should be converted into the 3-D aerosol composition. To do this, the differences between the ST-kriging AODs and background AODs (often called “observational increments”: $\Delta\text{AOD}_k = \text{AOD}_{\text{ST-kriging}, k} - \text{AOD}_{\text{bg}, k}$, $k = \text{grid cell}$) should be added to the background model-derived aerosol composition at each grid cell, in connection with the observation operators (Eq. (1)). Which aerosol species is/are selected for allocating ΔAOD_k ? We selected four types of control variables (CVs) of particulate species. First, all the particulate species were selected as CVs. In this case, ΔAOD_k was distributed to all the particulate species, with the particulate fractions calculated from the background CMAQ model simulations. The second CV was the selection of SO_4^{2-} concentration. Despite the large contribution of SO_4^{2-} to both AOD and PM concentration in East Asia, model-estimated SO_4^{2-} have shown large systematic underestimations, compared with observed SO_4^{2-} concentrations (Park et al., 2011, 2014b). This can be related to either (or both) the uncertainty in SO_2 emissions in East Asia or (and) the uncertainty in the parameterizations of SO_4^{2-} production in the CTM models (Kim et al., 2013; Lu et al., 2010; Smith et al., 2011; Park et al., 2014). In addition, there is also large

349 uncertainty in the levels of hydroxyl radicals (OH) due to uncertain daytime HONO chemistry,
 350 OH reactivation, in-plume process and others (Archibald et al., 2010; Han et al., 2015;
 351 Karamchandani et al., 2000; Kim et al., 2009; Kubistin et al., 2010; Lelieveld et al., 2008;
 352 Song et al., 2003, 2010; Sörgel et al., 2011; Stemmler et al., 2006; Zhou et al., 2011).
 353 Obviously, these uncertainties can influence the levels of H_2SO_4 and thus particulate sulfate
 354 concentrations in the atmosphere. In this case, aerosol mass concentrations (except for SO_4^{2-})
 355 were the same as those of the background aerosol concentrations. Third, SO_4^{2-} and OAs were
 356 chosen to be changed. Although OAs are one of the major particulate species, it is well-
 357 known that OAs concentrations are also systematically underestimated due to two reasons: (i)
 358 the uncertainty in the parameterizations of the OA formation (Donahue et al., 2006, 2011;
 359 Dzepina et al., 2009; Hodzic et al., 2010; Matsui et al., 2014; Slowik et al., 2010), and (ii) the
 360 uncertainty in emission inventories for anthropogenic and biogenic OA precursors (Guenther
 361 et al., 1999; Han et al., 2013; Sakulyanontvittaya et al., 2008; Tsimpidi et al., 2010; Wyat
 362 Appel et al., 2008). In this case, the mass concentration of surface OAs is assumed to be equal
 363 to that of SO_4^{2-} , based on the ground-based measurement studies over East Asia (Lee et al.,
 364 2009; Zhang et al., 2007, 2012). Finally, SO_4^{2-} , NO_3^- , NH_4^+ , and OAs were selected to be
 365 changed. In this case, ΔAOD_k was distributed to the selected four species, with the fractions
 366 of SO_4^{2-} , NO_3^- , NH_4^+ calculated from background simulations. The method to change the OA
 367 concentration in the fourth selection of CVs was the same as the method in the third selection
 368 of CVs. The fourth selection of CVs was also made to consider thermodynamic balance
 369 among SO_4^{2-} , NO_3^- , and NH_4^+ concentrations (Bassett and Seinfeld, 1983; Saxena et al., 1986;
 370 Seinfeld and Pandis, 2012; Song and Carmichael, 1999; Stelson et al., 1984). It should be
 371 noted that background modeling-derived vertical profiles and the size distributions of aerosol
 372 species were used for converting 2-D AOD to 3-D PM composition in all the STK cases.

With the combinations of the three different observation operators and four choices of CVs (Table 3), 12 hindcast runs were made for high PM episodes during the DRAGON-Asia campaign.

3 Results and Discussion

In Sect. 3, the performances of ST-kriging method are evaluated via comparisons with the AERONET AOD in the GOCI domain (Sect. 3.1). Sensitivity analyses were then conducted to examine the impacts of the observation operators and CVs on the accuracy of the hindcast runs (Sect. 3.2). After that, the overall performances of the hindcasts were evaluated with ground-based observations during the high PM₁₀ episodes over SMA (Sect. 3.3). A comparative analysis of the PM composition between hindcast results and observations was also conducted to further investigate/analyze the performance of the hindcast system (Sect. 3.4). In addition, hindcast results for the periods of less polluted episodes are also shown with the best configuration (Sect. 3.5).

3.1 Evaluation of ST-kriging AODs

Figure 5(a)-(c) show scatter plot analyses of background CMAQ-simulated AODs, spatial kriging AODs (i.e., kriging only with the GOCI AODs from one scene) and ST-kriging AODs vs. AERONET level 2 AODs over the GOCI domain during the DRAGON-Asia campaign. First, it can be found that the CMAQ-predicted AODs are underestimated significantly compared with the AERONET AODs. As discussed in Sect. 2.3, this was the main reason that we used the ST-kriging method in this study. More weight should be given to observations, because the CTM modelling produces significant biases. Second, ST-kriging AODs show improved correlations, compared with the AODs estimated via the spatial kriging method.

Also, the ST-kriging AOD data show equivalent levels of errors and biases, compared with GOCI AOD data. If one compares Fig. 3(b) with Fig. 5(c), it can be seen that the ST-kriging can effectively produce the AOD fields (also note the increase in N).

Figures 5(d) and (e) show the scatter plot analysis of the ST-kriging AOD products versus the AERONET AOD data with kriging variances (KVs). It is found that the ST-kriging AOD data with $KV \leq 0.04$ show similar scattering pattern and accuracy to those of GOCI AOD. In contrast, some overestimated outliers from the ST-kriging AOD data in Fig. 5(e) (e.g., 1.0-2.0 in the x-axis and 2.0-4.0 in the y-axis) show different patterns than those from the GOCI AOD data. This may be explained by the relatively large KVs (> 0.04) of such overestimated outliers. The KV generally increases when the observations near a certain prediction point are not available or when nearby observations have relatively large errors. Thus, when the GOCI observations are contaminated by optically thin clouds and they are not removed perfectly, this can increase the local variances due to their high cloud optical depth (COD). These factors can affect the quality of the ST-kriging AOD products. In this study, only the ST-kriging AOD products having small KVs (less than 0.04) were used for preparing the initial condition of each data processing step. Therefore, the initial PM concentrations did not changed where the ST-kriging AOD having large KVs (larger than 0.04). Collectively, it appears that the ST-kriging method is a reasonable tool for obtaining realistic AOD values at locations where the GOCI observations are not available.

3.2 Sensitivity of observation operators and control variables to AOD and PM₁₀ predictions

To investigate the best combination of the observation operators and CVs, the AOD and PM₁₀ hindcast runs and sensitivity analyses with the 12 different configurations (Table 3) were performed. For this, the hindcast AOD and PM₁₀ from 13:00 LT to 19:00 LT (H+1 to H+6) on 10 selected episode days were compared with the ground-measured AOD and surface PM₁₀. The observations from the six AERONET sites and nearest NAMIS PM₁₀ stations within 10 km from the AERONET locations were selected for this comparison study (Fig. 2). The AOD values for the background CMAQ model simulations without the application of the ST-kriging method (noSTK) were also calculated with the GEOS-Chem observation operator.

Figure 6 shows the soccer plot analysis of the 13 hindcast AODs (left panel) and PM₁₀ (right panel) during the first 6-h of the short-term PM hindcasting on the 10 selected episode days. In the soccer plot, mean fractional bias (MFB) and mean fractional error (MFE) (described in Appendix B) are plotted on the x- and y-axes, respectively. Using this plot, the relative discrepancy can be presented by the distances from the origin of the plot, and particular characteristic, such as systematic bias, can also be shown as a group of scatter points. Detailed statistical metric values are shown in Table 4. All the AODs and PM₁₀ with the application of the ST-kriging method (STK) are much better than those from the noSTK simulation, with reduced errors and biases. Percentage decreases in MFE with the STK hindcasts were found to be 60-67% for AOD and are 50-63% for PM₁₀. The MFB also decreased by 67-82% for AOD and by 56-84% for PM₁₀. The noSTK case showed a strong negative bias (i.e., underprediction) and the 12 STK cases also showed less, yet still negative, biases. These negative biases are considered to be systematic, because of the negative bias of the GOCI AOD data (Fig. 6). Additionally, the negative biases are due to underestimation of CMAQ-

simulated SO_4^{2-} and OAs concentrations (Carlton et al., 2008, 2010; Park et al., 2011, 2014b).

This issue has been discussed in Sect. 2.5 and is investigated further in Sect. 3.4.

On the other hand, there are relatively small differences in errors and biases among the 12 STK cases (Fig. 6). Several differences among the 12 sensitivity cases were investigated further. First, the error and bias patterns for the AOD values were different from those for the PM_{10} predictions, being associated with the different observation operators. For example, the STK cases with the IMPROVE observation operator (cases C1, C2, C3, and C4) exhibited a relatively small bias for PM_{10} predictions, although they did not in the AOD predictions. This was likely caused by small **wet** MEE values of SO_4^{2-} , NO_3^- , and NH_4^+ in the IMPROVE observation operator (represented by the green line in Fig. 4). By Eq. (1), the concentrations of converted aerosol species are inversely proportional to the MEEs of aerosol species. In the CV cases, the selections of SO_4^{2-} and OAs (i.e., A3, B3, and C3) and SO_4^{2-} , NO_3^- , NH_4^+ , and OAs (i.e., A4, B4, and C4) showed better performances for both the AOD and PM_{10} predictions.

To show the degree of enhanced performances via using the ST-kriging GOCI data, we also carried out some hindcast simulations, using the initial conditions prepared with single-frame GOCI data at 11:30 LT. The grids that did not have AOD observations were not filled out in this runs. In Fig. 6, the MFBs and MFEs of the bilinear interpolation method (denoted as BL) were -45.05 and 59.52 for AOD and -46.13 and 53.30 for PM_{10} , respectively. It is shown in Fig. 6 that the use of the single-frame GOCI data without filling any gap cannot sufficiently improve the performance, compared with the cases of the STK simulations.

Figure 7 shows the performances of the short-term hindcast system with the 13 different configurations via comparisons between the hourly-averaged PM_{10} observations and model PM_{10} predictions at the six NAMIS sites, on 9 April, 6 May and 16 May, 2012, respectively.

Only 3-day and six-site results were selected and presented here, and more comprehensive performance evaluations are presented in Sect. 3.3. While noSTK failed to reproduce the high PM pollutions, all the STK cases showed significant improvements in the surface PM₁₀ predictions. However, there was a tendency that the hourly peaks of PM₁₀ were not well captured by the STK cases.

Consequently, it can be concluded that the combination of GOCART observation operator and CVs of SO₄²⁻ and OAs (represented by A3) leads to the best results in the current hindcast system (Table 4). The use of the GOCART observation operator and CVs of SO₄²⁻, NO₃⁻, NH₄⁺, and OAs (represented by A4) could also provide comparable performance to A3. However, it appears that the differences among the 12 STK cases were relatively small.

3.3 Overall performance evaluation of PM₁₀ hindcast over SMA

In this section, PM₁₀ from the hindcast experiments were compared with the PM₁₀ observations from “58 NAMIS sites” to evaluate the overall performance of the current hindcast system in SMA. Table 5 provides the statistical metrics that were calculated separately from the first and the second 6-h hindcast results. The main characteristics of the statistical analysis in Table 5 are similar to those at the six sites discussed in the previous section. First, both errors and biases of PM₁₀ distributions were significantly reduced after the application of the ST-kriging method. The MFEs and MFBs in the 12-h STK simulations decreased by ~40% and ~80%, respectively.

A distinctive difference was also found in the model performances for the first and the second 6-h runs. During the first 6-h, all the hindcast results showed negative biases, with the MFB of ~ -100% for the noSTK cases and ~ -40% for the STK cases. The performances of the A3 and A4 cases are somewhat better than those of the other STK cases (Table 5). Collectively,

the MFEs and MFBs of the STK cases are a factor of 2-4 smaller than those of the noSTK cases during the first 6-h.

Figure 8 shows a comparison between the noSTK case and the A3 case, in terms of the PM_{10} predictions, during the first and the next 6 h in SMA with the 6-h averaged NAMIS PM_{10} observations. As shown, the A3 case produced better PM_{10} predictions during the first and the next 6 h. In addition, the A4 case (not shown) also provided similar results to the A3 case, as discussed in Sect. 3.2. It can be confirmed again that the A3 and A4 cases are able to produce better PM_{10} predictions against the PM_{10} observations in SMA.

Hindcast performances from H+13 to H+24 were also evaluated with the ground-measured NAMIS PM_{10} data. In short, the differences between all the STK and noSTK cases became smaller than those during the first 12 h (approximate difference of 10% was found at H+24, i.e., 24 h after the hindcast actually began). Based on this, it appears that the effects of using the initial PM composition on the hindcast performances may effectively last during the first 12 h. After 12 h, the effects started to diminish. This is due to several facts: (i) the regions for applying the initial PM composition in this study were limited only within the GOCI domain (relatively small region); (ii) although the initial PM composition was used, its effects can be offset by uncertainties and errors in emissions as time progressed; and (iii) the large uncertainties associated with the formation of SO_4^{2-} and OAs in the CTMs can also limit the effects of the initial PM composition. The second and the third are the reasons that there is strong necessity for both emissions and CTMs to be improved continuously, even though the initial PM composition is applied in the short-term forecast activities.

3.4 Evaluation of hindcast performance with observed PM composition

In the previous section, PM_{10} mass concentrations were simply predicted by the short-term hindcast system with 12 different combinations of observation operators and CVs. Although the purpose of this study is to develop a better PM forecast system for accurately predicting “ PM_{10} mass” concentrations, it is still necessary to more carefully scrutinize the changes in the “PM composition” in accordance with the different selections of the CVs.

During the DRAGON-Asia campaign, the $\text{PM}_{2.5}$ composition was measured for SO_4^{2-} , NO_3^- , and NH_4^+ with 30-min intervals and for SO_4^{2-} , NO_3^- , NH_4^+ , OC and BC with 24-h intervals using PILS-IC instrument (semi-continuous measurements) and low air-volume sampler with a Teflon filter (off-line measurements), respectively, in Yongin City near SMA (Fig. 2). Thus, in this section, the selection of the CVs is further discussed with the observed $\text{PM}_{2.5}$ composition.

Figure 9 shows the comparison between 1-h averaged SO_4^{2-} , NO_3^- , and NH_4^+ concentrations measured via the PILS-IC instrument and model-predicted concentrations during the selected days at the Yongin observation site. Only the STK cases with the GOCART observation operator (i.e., A1, A2, A3, and A4) were selected here. The STK cases showed significant changes in the PM composition with the selection of CVs. For example, the A2 and A3 cases tended to overestimate the SO_4^{2-} concentrations but underestimated the NO_3^- and NH_4^+ concentrations, whereas the A1 and A4 cases tended to relatively well capture the trend of the concentrations of the three particulate species. This phenomenon was driven by intra-particulate thermodynamics. That is, if larger amounts of SO_4^{2-} are allocated into particles (like the cases of A2 and A3), then NO_3^- tends to be evaporated, because SO_4^{2-} is more strongly associated with NH_4^+ (Song and Carmichael, 1999). As shown in Fig. 9 (a) and (b), when the SO_4^{2-} concentrations increases (as in case A2), the NO_3^- concentrations decrease

accordingly, because NO_3^- is evaporated out of the particulate phase as a form of HNO_3 (Song and Carmichael, 1999, 2001). Collectively, the “best” results were produced from the case A4, as shown in Figs. 9(a)-(c).

The 24-h averaged $\text{PM}_{2.5}$ compositions measured from the PILS-IC instrument and the low air-volume sampler with a Teflon filter during the campaign period are also compared in Fig. 9(d). Again, the observations of the SO_4^{2-} , NO_3^- , and NH_4^+ concentrations were obtained from both the PILS-IC instrument and the low volume sampler, whereas the concentrations of OAs ($\cong [\text{OC}] \times 1.5$) and EC were only measured via the low air-volume sampler. As shown in Fig. 9(d), the SO_4^{2-} , NO_3^- , and NH_4^+ concentrations from both samplers showed good agreements (see circles and crosses in Fig. 9(d)). The A4 case (the red bars in Fig. 9(d)) again showed the best results in the comparison between the observed and predicted particulate composition, particularly in SO_4^{2-} and OAs. In the previous discussion (see Sect. 3.2 and 3.3), the A3 and A4 cases showed the best performances for predicting “ PM_{10} mass concentrations” over SMA. This is somewhat consistent with our analysis in this section. However, in case of the A3, it can capture the PM mass behaviors (Sect. 3.3) but does not capture the changes in the PM composition well (this section). Based on this, it is concluded that the A4 case would be the best configuration for accurately predicting the PM composition as well as the PM mass. However, this PM composition analysis was conducted with only one site observations (Yongin City) in this study. Thus, to reach a firmer conclusion, more intensive analyses with multiple site observations are required in future.

3.5 Evaluation of short-term hindcast performances

To further evaluate the performance of the short-term hindcast runs, 48-hour hindcast simulations with the configuration of A4 were carried out from 7 March to 19 March. The

observations from the 6 AERONET sites and the nearest NAMIS stations were analyzed in this study.

The time-series of the first and the second 24-hour averaged PM_{10} at the six sites on 8, 10, and 11 March, 2012 are presented in Fig. 10. Again, reduced errors and biases were shown in the A4 STK simulations, compare with the noSTK simulation for polluted episodes ((a) and (b) in Fig. 10) and for less polluted episode ((c) in Fig. 10). Percent decreases with MFEs of the first 24-hour A4 STK hindcast were ~40% for AOD and ~10% for PM_{10} , and those with MFBs were ~40% for AOD and ~100% for PM_{10} . In addition, slight improvements in the horizontal distributions of AOD and PM_{10} were also found. This was indicated by the increases of correlation coefficients (refer to Table S1). The second 24-hour STK hindcasts also reduced the errors and biases for AOD and PM_{10} , although the improvements in the spatial distributions were not shown clearly. A more detailed statistical metrics is presented in the supplement (Table S1).

4 Summary and Conclusions

For the purpose of improving the performance of short-term PM forecast in Korea, an integrated air quality modeling system was developed with the application of the ST-kriging method using the geostationary satellite-derived AOD data over Northeast Asia. The errors and biases of the ST-kriging AOD showed relatively good agreement, compared with the AERONET observations. With the combinations of the ST-kriging method along with various observation operators and control variables (CVs), the errors and biases of AOD and PM_{10} predictions can be reduced significantly. It was shown that the selection of the observation operators greatly influence the performances of the STK hindcast systems. On the other hand, the choice of CVs tends to affect PM composition. The combination of the GOCART

observation operator and the selection of CVs of SO_4^{2-} and OAs (case A3) was found to be the best one for the PM_{10} mass prediction. All the hindcast runs with the application of the ST-kriging, however, generally showed negative biases (i.e. under-predictions). This was primarily due to the underestimation of the GOCI AOD.

Reducing errors and biases in the current system is important for further development of the PM forecast system. One of the potential methods for reducing the errors and biases is to introduce the MODIS AOD data into the ST-kriging stage, together with the GOCI data. It is expected that this will be able to further reduce the systematic biases, due to the relatively small biases of MODIS AOD (as shown Fig. 3). In addition, the combination of the GOCART observation operator and the selection of CVs of SO_4^{2-} , NO_3^- , NH_4^+ , and OAs (Case A4) was found to give the “best” results for the prediction of particulate composition at one observation site. However, more intensive measurements of the PM composition are needed for reaching a more solid conclusion.

The ST-kriging AODs used in the current study are expected to be used in other data assimilation methods. For example, in the 3DVAR method, the observation error covariance matrix, which presents the degree of errors of the observations, has been usually assumed by linear equations or single constant value (Liu et al., 2011; Schwartz et al., 2012; Shi et al., 2011). However, as discussed with KVs in Sect. 3.1, the error covariance of the AOD observations can be improved, and the use of the improved observation error covariance matrix can help to prepare more accurate AOD fields, for example, via a 3DVAR method. This study is now underway.

In future, planned GEO satellite sensors will give other opportunities to use semi-continuous AOD observations at high spatial and temporal resolutions. Upcoming GEO satellite sensors scheduled for launch between 2018 and 2020 include NASA’s Tropospheric Emissions:

603 Monitoring of Pollution (TEMPO) over North America, ESA's Sentinel-4 over Europe, and
604 Korea Aerospace Research Institute (KARI)'s Geostationary Environment Monitoring
605 Spectrometer (GEMS) over Asia. In the case of the GEMS instrument, it is being designed to
606 provide backscattered UV/Vis radiances between 300 and 500 nm with a spatial resolution of
607 $5 \text{ km} \times 5 \text{ km}$ over a large part of Asia. Using advanced observations from the GEMS sensor,
608 it is anticipated that the system developed here will be able to make significant contributions
609 to further improvements in the performances of the PM forecasting system in Asia. This
610 improved PM predictions and modeling framework can also be a core part for entire air
611 quality forecasting system, a more comprehensive health impact assessments, and radiative
612 forcing estimation over (East) Asia in future.

613

614 **Appendix A: Spatio-temporal kriging method**

615 The ST-kriging methods assume that measured variables in space and time ($\tau(s, t)$) can be
616 regarded as a random function, consisting of a trend component (m) and residual component
617 (ϵ) of which the mean is zero:

$$618 \quad \tau(s, t) = m(s, t) + \epsilon(s, t) . \quad (\text{A1})$$

619 The unobserved value $\tau^*(s, t)$ can be averaged with weight using measured values from the
620 surrounding:

$$621 \quad \tau^*(s, t) = \sum_{i=1}^n \tau(s_i, t_i) w_i(s, t) \quad (\text{A2})$$

622 where n is the number of observations in local neighborhood and $w_i(s, t)$ is the kriging weight
623 assigned to $\tau(s_i, t_i)$. The kriging weight is determined by a theoretical semivariogram.

624 In case of spatial kriging ($\tau(s)$), the semivariogram (γ) is the best fit to the semivariance (γ^*) as
 625 a function of spatial lag (h). Assuming the trend component $m(s)$ in $\tau(s)$ is constant over the
 626 local domain (i.e., the ordinary kriging method), the semivariance is defined as:

$$627 \quad \gamma^*(h) = \frac{1}{2N(h)} \sum_{i=1}^{N(h)} [\tau(s_i) - \tau(s_i + h)]^2 = \frac{1}{2N(h)} \sum_{i=1}^{N(h)} [\varepsilon(s_i) - \varepsilon(s_i + h)]^2 \quad (\text{A3})$$

628 where $N(h)$ is the number of paired observations at a spatial distance of h , and $\tau_i(s_i + h)$ is the
 629 i th observation (in this study, AOD) separated by h from the observation located at s_i . The
 630 semivariogram is then depicted by a theoretical model which is the best-fitting curve to the
 631 semivariance by minimizing the least square error. For example, a spherical semivariogram
 632 (γ), which is commonly used in the theoretical models of the atmospheric studies, is estimated
 633 by finding optimal three parameters: (i) nugget (c_n); (ii) range (a); and (iii) partial sill (σ_0^2):

$$634 \quad \gamma(h) = c_n + \sigma_0^2 \left[\frac{3h}{2a} - \frac{h^3}{2a^3} \right] \quad (\text{for } h \leq a), \quad \gamma(h) = c_n + \sigma_0^2 \quad (\text{for } h > a). \quad (\text{A4})$$

635 The range parameter indicates the maximum lag in which the variation of semivariogram is
 636 meaningful (Cressie, 1992).

637 To combine the spatial and temporal data for preparing the spatio-temporal semivariograms,
 638 the temporal information can be converted into the spatial information (Gräler et al. (2012)).
 639 First, the spatial and temporal semivariograms are estimated independently using the spherical
 640 model from the daily GOCI AOD data. Second, the ratio of spatial range parameter (a_s) of the
 641 spatial semivariogram to temporal range parameter (a_t) of the temporal semivariogram (i.e.,
 642 spatio-temporal scale factor, km h^{-1}) is used to convert the unit of temporal lag into the unit of
 643 spatial distance. Consequentially, the 3D spatio-temporal AOD data are converted into the 2-
 644 D spatial AOD fields. After that, the spatio-temporal semivariogram is provided to predict the
 645 AOD fields with $15 \text{ km} \times 15 \text{ km}$ spatial resolution from 10:00 LT to 16:00 LT over the GOCI

domain. For the ST-kriging method, the “gstat” (Pebesma, 2004) and the “spacetime” (Pebesma, 2012) software packages in the “R” environment for statistical computing were used (R Development Core Team, 2011). Figure A1 presents an example of the 3D semivariograms from the fitted model (left) and sample from the GOCI data on 8 April. The mean nugget (c_n), range (a), partial sill (σ_0^2) of the spatio-temporal model semivariogram were 0.025, 583km, and 0.227, respectively, during the entire DRAGON-Asia campaign. The average spatio-temporal scale factor of $\sim 34 \text{ km h}^{-1}$ was calculated indicating that the AODs observed before or after 1 h at certain location show a similar correlation pattern to those measured simultaneously at $\sim 34 \text{ km}$ apart in the ST-kriging model. **Figure A2 shows an example of spatial distributions of GOCI AOD from 10:30 to 13:30 LT and ST-kriging AOD at 12:00 LT with a criteria of kriging variances (KVs) less than 0.04.**

Appendix B: Statistical metrics

In this study, eight statistical metrics were used for validating the hindcast results (Chai and Draxler, 2014; Savage et al., 2013; Willmott, 1981; Willmott et al., 2009; Willmott and Matsuura, 2005).

$$\text{Index of agreement (IOA)} = 1 - \frac{\sum_{i=1}^N (O_i - M_i)^2}{\sum_{i=1}^N (|O_i - \overline{O}| + |M_i - \overline{M}|)^2} \quad (\text{B1})$$

$$\text{Mean fractional error (MFE)} = \frac{1}{N} \sum_{i=1}^N \frac{|M_i - O_i|}{\left(\frac{M_i + O_i}{2}\right)} \times 100 \quad (\text{B2})$$

$$\text{Mean fractional bias (MFB)} = \frac{1}{N} \sum_{i=1}^N \frac{(M_i - O_i)}{\left(\frac{M_i + O_i}{2}\right)} \times 100 \quad (\text{B3})$$

$$\text{Regression coefficient (R)} = \frac{\sum_{i=1}^N (O_i - \overline{O_i})(M_i - \overline{M_i})}{\sqrt{\sum_{i=1}^N (O_i - \overline{O_i})^2} \sqrt{\sum_{i=1}^N (M_i - \overline{M_i})^2}} \quad (\text{B4})$$

$$\text{Root mean square error (RMSE)} = \sqrt{\frac{1}{N} \sum_{i=1}^N (M_i - O_i)^2} \quad (\text{B5})$$

$$\text{Mean normalized error (MNE)} = \frac{1}{N} \sum_{i=1}^N \left(\frac{|M_i - O_i|}{O_i} \right) \times 100 \quad (\text{B6})$$

$$\text{Mean bias (MB)} = \frac{1}{N} \sum_{i=1}^N (M_i - O_i) \quad (\text{B7})$$

$$\text{Mean Normalized bias (MNB)} = \frac{1}{N} \sum_{i=1}^N \left(\frac{M_i - O_i}{O_i} \right) \times 100 \quad (\text{B8})$$

where N is the number of data and M_i and O_i are the model value and observation, respectively. The value highlighted by overbar means the arithmetic mean of the data.

Code Availability

WRF and CMAQ source codes and R and NCL computer languages are available to the public. The source codes and computer languages may be downloaded by following instructions found at:

<http://www2.mmm.ucar.edu/wrf/users/downloads.html> for WRF,

<https://www.cmascenter.org/cmaq> for CMAQ,

<http://cran.r-project.org> for R, and

<https://www.ncl.ucar.edu/Download> for NCL.

681 ST-kriging module code used in this study was based on the instruction of Pebesma (2012)
682 available at <http://www.jstatsoft.org/v51/i07>, and can be obtained by contacting S. Lee
683 (noitul5@gist.ac.kr).

684

685 **Acknowledgements**

686 This research was supported by the GEMS program of the Ministry of Environment, South
687 Korea, as part of the Eco Innovation Program of KEITI (2012000160004). **This work was**
688 **also funded by the Korea Meteorological Administration Research and Development Program**
689 **under Grant KMIPA 2015-5010. We also thank all PI investigators and their staff for**
690 **establishing and maintaining the AERONET sites of DRAGON-NE Asia 2012 campaign used**
691 **in this study. We also thank the MODIS science team for providing valuable data for this**
692 **research.** NCL (2014) was used to draw the figures. The third author is supported by the R&D
693 project on the development of global numerical weather prediction systems of Korea Institute
694 of Atmospheric Prediction Systems (KIAPS) funded by Korea Meteorological Administration
695 (KMA).
696

697 **References**

- 698 Archibald, A. T., Cooke, M. C., Utembe, S. R., Shallcross, D. E., Derwent, R. G. and Jenkin,
699 M. E.: Impacts of mechanistic changes on HO_x formation and recycling in the oxidation of
700 isoprene, *Atmos. Chem. Phys.*, 10(17), 8097–8118, doi:10.5194/acp-10-8097-2010, 2010.
- 701 Bassett, M. and Seinfeld, J. H.: Atmospheric equilibrium model of sulfate and nitrate aerosols,
702 *Atmos. Environ.* 1967, 17(11), 2237–2252, doi:10.1016/0004-6981(83)90221-4, 1983.
- 703 Benedetti, A., Morcrette, J.-J., Boucher, O., Dethof, A., Engelen, R. J., Fisher, M., Flentje, H.,
704 Huneus, N., Jones, L., Kaiser, J. W., Kinne, S., Mangold, A., Razinger, M., Simmons, A. J.
705 and Suttie, M.: Aerosol analysis and forecast in the European Centre for Medium-Range
706 Weather Forecasts Integrated Forecast System: 2. Data assimilation, *J. Geophys. Res.*
707 *Atmospheres*, 114(D13), D13205, doi:10.1029/2008JD011115, 2009.
- 708 Brook, R. D., Rajagopalan, S., Pope, C. A., Brook, J. R., Bhatnagar, A., Diez-Roux, A. V.,
709 Holguin, F., Hong, Y., Luepker, R. V., Mittleman, M. A., Peters, A., Siscovick, D., Smith, S.
710 C., Whitsel, L. and Kaufman, J. D.: Particulate Matter Air Pollution and Cardiovascular
711 Disease An Update to the Scientific Statement From the American Heart Association,
712 *Circulation*, 121(21), 2331–2378, doi:10.1161/CIR.0b013e3181dbee1, 2010.
- 713 Brunekreef, B. and Holgate, S. T.: Air pollution and health, *The Lancet*, 360(9341), 1233–
714 1242, doi:10.1016/S0140-6736(02)11274-8, 2002.
- 715 Byun, D. and Schere, K. L.: Review of the governing equations, computational algorithms,
716 and other components of the models-3 Community Multiscale Air Quality (CMAQ) modeling
717 system, *Appl. Mech. Rev.*, 59(1-6), 51–76, doi:10.1115/1.2128636, 2006.
- 718 Byun, D. W. and Ching, J. K. S.: Science algorithms of the EPA Models-3 community
719 multiscale air quality (CMAQ) modeling system, 1999.
- 720 Carlton, A. G., Turpin, B. J., Altieri, K. E., Seitzinger, S. P., Mathur, R., Roselle, S. J. and
721 Weber, R. J.: CMAQ Model Performance Enhanced When In-Cloud Secondary Organic
722 Aerosol is Included: Comparisons of Organic Carbon Predictions with Measurements,
723 *Environ. Sci. Technol.*, 42(23), 8798–8802, doi:10.1021/es801192n, 2008.

724 Carlton, A. G., Bhawe, P. V., Napelenok, S. L., Edney, E. O., Sarwar, G., Pinder, R. W.,
 725 Pouliot, G. A. and Houyoux, M.: Model Representation of Secondary Organic Aerosol in
 726 CMAQv4.7, *Environ. Sci. Technol.*, 44(22), 8553–8560, doi:10.1021/es100636q, 2010.

727 Chai, T. and Draxler, R. R.: Root mean square error (RMSE) or mean absolute error (MAE)?
 728 – Arguments against avoiding RMSE in the literature, *Geosci. Model Dev.*, 7(3), 1247–1250,
 729 doi:10.5194/gmd-7-1247-2014, 2014.

730 Chin, M., Ginoux, P., Kinne, S., Torres, O., Holben, B. N., Duncan, B. N., Martin, R. V.,
 731 Logan, J. A., Higurashi, A. and Nakajima, T.: Tropospheric Aerosol Optical Thickness from
 732 the GOCART Model and Comparisons with Satellite and Sun Photometer Measurements, *J.*
 733 *Atmospheric Sci.*, 59(3), 461–483, doi:10.1175/1520-
 734 0469(2002)059<0461:TAOTFT>2.0.CO;2, 2002.

735 Choi, M., Kim, J., Lee, J., Kim, M., Je Park, Y., Jeong, U., Kim, W., Holben, B., Eck, T. F.,
 736 Lim, J. H., and Song, C. K.: GOCI Yonsei Aerosol Retrieval (YAER) algorithm and
 737 validation during DRAGON-NE Asia 2012 campaign, *Atmos. Meas. Tech. Discuss.*, 8, 9565-
 738 9609, doi:10.5194/amtd-8-9565-2015, 2015.

739 Cressie, N.: Statistics for Spatial Data, *Terra Nova*, 4(5), 613–617, doi:10.1111/j.1365-
 740 3121.1992.tb00605.x, 1992.

741 Denby, B., Schaap, M., Segers, A., Builtjes, P. and Horálek, J.: Comparison of two data
 742 assimilation methods for assessing PM₁₀ exceedances on the European scale, *Atmos. Environ.*,
 743 42(30), 7122–7134, doi:10.1016/j.atmosenv.2008.05.058, 2008.

744 Donahue, N. M., Robinson, A. L., Stanier, C. O. and Pandis, S. N.: Coupled Partitioning,
 745 Dilution, and Chemical Aging of Semivolatile Organics, *Environ. Sci. Technol.*, 40(8), 2635–
 746 2643, doi:10.1021/es052297c, 2006.

747 Donahue, N. M., Epstein, S. A., Pandis, S. N. and Robinson, A. L.: A two-dimensional
 748 volatility basis set: 1. organic-aerosol mixing thermodynamics, *Atmos. Chem. Phys.*, 11(7),
 749 3303–3318, doi:10.5194/acp-11-3303-2011, 2011.

750 Dzepina, K., Volkamer, R. M., Madronich, S., Tulet, P., Ulbrich, I. M., Zhang, Q., Cappa, C.
 751 D., Ziemann, P. J. and Jimenez, J. L.: Evaluation of recently-proposed secondary organic
 752 aerosol models for a case study in Mexico City, *Atmos. Chem. Phys.*, 9(15), 5681–5709,
 753 doi:10.5194/acp-9-5681-2009, 2009.

754 Fishman, J., Iraci, L. T., Al-Saadi, J., Chance, K., Chavez, F., Chin, M., Coble, P., Davis, C.,
755 DiGiacomo, P. M., Edwards, D., Eldering, A., Goes, J., Herman, J., Hu, C., Jacob, D. J.,
756 Jordan, C., Kawa, S. R., Key, R., Liu, X., Lohrenz, S., Mannino, A., Natraj, V., Neil, D., Neu,
757 J., Newchurch, M., Pickering, K., Salisbury, J., Sosik, H., Subramaniam, A., Tzortziou, M.,
758 Wang, J. and Wang, M.: The United States' Next Generation of Atmospheric Composition
759 and Coastal Ecosystem Measurements: NASA's Geostationary Coastal and Air Pollution
760 Events (GEO-CAPE) Mission, *Bull. Am. Meteorol. Soc.*, 93(10), 1547–1566,
761 doi:10.1175/BAMS-D-11-00201.1, 2012.

762 Friedl, M. A., McIver, D. K., Hodges, J. C. F., Zhang, X. Y., Muchoney, D., Strahler, A. H.,
763 Woodcock, C. E., Gopal, S., Schneider, A., Cooper, A., Baccini, A., Gao, F. and Schaaf, C.:
764 Global land cover mapping from MODIS: algorithms and early results, *Remote Sens.*
765 *Environ.*, 83(1–2), 287–302, doi:10.1016/S0034-4257(02)00078-0, 2002.

766 Gräler, B., Gerharz, L. and Pebesma, E.: Spatio-temporal analysis and interpolation of PM₁₀
767 measurements in Europe, [online] Available from:
768 http://acm.eionet.europa.eu/reports/ETCACM_TP_2011_10_spatio-temp_AQinterpolation,
769 2012.

770 Guenther, A., Baugh, B., Brasseur, G., Greenberg, J., Harley, P., Klinger, L., Serça, D. and
771 Vierling, L.: Isoprene emission estimates and uncertainties for the central African
772 EXPRESSO study domain, *J. Geophys. Res. Atmospheres*, 104(D23), 30625–30639,
773 doi:10.1029/1999JD900391, 1999.

774 Guenther, A., Karl, T., Harley, P., Wiedinmyer, C., Palmer, P. I. and Geron, C.: Estimates of
775 global terrestrial isoprene emissions using MEGAN (Model of Emissions of Gases and
776 Aerosols from Nature), *Atmos. Chem. Phys.*, 6(11), 3181–3210, doi:10.5194/acp-6-3181-
777 2006, 2006.

778 Han, K. M., Park, R. S., Kim, H. K., Woo, J. H., Kim, J. and Song, C. H.: Uncertainty in
779 biogenic isoprene emissions and its impacts on tropospheric chemistry in East Asia, *Sci. Total*
780 *Environ.*, 463-464, 754–771, doi:10.1016/j.scitotenv.2013.06.003, 2013.

781 Han, K. M., Lee, S., Chang, L. S. and Song, C. H.: A comparison study between CMAQ-
782 simulated and OMI-retrieved NO₂ columns over East Asia for evaluation of NO_x emission
783 fluxes of INTEX-B, CAPSS, and REAS inventories, *Atmos. Chem. Phys.*, 15(4), 1913–1938,
784 doi:10.5194/acp-15-1913-2015, 2015.

785 He, L.-Y., Huang, X.-F., Xue, L., Hu, M., Lin, Y., Zheng, J., Zhang, R. and Zhang, Y.-H.:
 786 Submicron aerosol analysis and organic source apportionment in an urban atmosphere in
 787 Pearl River Delta of China using high-resolution aerosol mass spectrometry, *J. Geophys. Res.*,
 788 116(D12), doi:10.1029/2010JD014566, 2011.

789 Hodzic, A., Jimenez, J. L., Madronich, S., Canagaratna, M. R., DeCarlo, P. F., Kleinman, L.
 790 and Fast, J.: Modeling organic aerosols in a megacity: potential contribution of semi-volatile
 791 and intermediate volatility primary organic compounds to secondary organic aerosol
 792 formation, *Atmos. Chem. Phys.*, 10(12), 5491–5514, doi:10.5194/acp-10-5491-2010, 2010.

793 Holben, B. N., Eck, T. F., Slutsker, I., Tanré, D., Buis, J. P., Setzer, A., Vermote, E., Reagan,
 794 J. A., Kaufman, Y. J., Nakajima, T., Lavenu, F., Jankowiak, I. and Smirnov, A.:
 795 AERONET—A Federated Instrument Network and Data Archive for Aerosol
 796 Characterization, *Remote Sens. Environ.*, 66(1), 1–16, doi:10.1016/S0034-4257(98)00031-5,
 797 1998.

798 Huang, X.-F., He, L.-Y., Hu, M., Canagaratna, M. R., Sun, Y., Zhang, Q., Zhu, T., Xue, L.,
 799 Zeng, L.-W., Liu, X.-G., Zhang, Y.-H., Jayne, J. T., Ng, N. L. and Worsnop, D. R.: Highly
 800 time-resolved chemical characterization of atmospheric submicron particles during 2008
 801 Beijing Olympic Games using an Aerodyne High-Resolution Aerosol Mass Spectrometer,
 802 *Atmos. Chem. Phys.*, 10(18), 8933–8945, doi:10.5194/acp-10-8933-2010, 2010.

803 Karamchandani, P., Santos, L., Sykes, I., Zhang, Y., Tonne, C. and Seigneur, C.:
 804 Development and Evaluation of a State-of-the-Science Reactive Plume Model, *Environ. Sci.*
 805 *Technol.*, 34(5), 870–880, doi:10.1021/es990611v, 2000.

806 Kim, H. S., Song, C. H., Park, R. S., Huey, G. and Ryu, J. Y.: Investigation of ship-plume
 807 chemistry using a newly-developed photochemical/dynamic ship-plume model, *Atmos. Chem.*
 808 *Phys.*, 9(19), 7531–7550, doi:10.5194/acp-9-7531-2009, 2009.

809 Kim, H. S., Kim, Y. H. and Song, C. H.: Ship-plume sulfur chemistry: ITCT 2K2 case study,
 810 *Sci. Total Environ.*, 450-451, 178–187, doi:10.1016/j.scitotenv.2013.01.099, 2013.

811 Kubistin, D., Harder, H., Martinez, M., Rudolf, M., Sander, R., Bozem, H., Eerdekens, G.,
 812 Fischer, H., Gurk, C., Klüpfel, T., Königstedt, R., Parchatka, U., Schiller, C. L., Stickler, A.,
 813 Taraborrelli, D., Williams, J. and Lelieveld, J.: Hydroxyl radicals in the tropical troposphere

814 over the Suriname rainforest: comparison of measurements with the box model MECCA,
 815 Atmos. Chem. Phys., 10(19), 9705–9728, doi:10.5194/acp-10-9705-2010, 2010.

816 Lahoz, W. A., Peuch, V.-H., Orphal, J., Attié, J.-L., Chance, K., Liu, X., Edwards, D., Elbern,
 817 H., Flaud, J.-M., Claeysman, M. and Amraoui, L. E.: Monitoring Air Quality from Space: The
 818 Case for the Geostationary Platform, Bull. Am. Meteorol. Soc., 93(2), 221–233,
 819 doi:10.1175/BAMS-D-11-00045.1, 2011.

820 Lee, J., Kim, J., Song, C. H., Ryu, J.-H., Ahn, Y.-H. and Song, C. K.: Algorithm for retrieval
 821 of aerosol optical properties over the ocean from the Geostationary Ocean Color Imager,
 822 Remote Sens. Environ., 114(5), 1077–1088, doi:10.1016/j.rse.2009.12.021, 2010.

823 Lee, J., Kim, J., Yang, P. and Hsu, N. C.: Improvement of aerosol optical depth retrieval from
 824 MODIS spectral reflectance over the global ocean using new aerosol models archived from
 825 AERONET inversion data and tri-axial ellipsoidal dust database, Atmos. Chem. Phys., 12(15),
 826 7087–7102, doi:10.5194/acp-12-7087-2012, 2012.

827 Lee, S., Ghim, Y. S., Kim, S.-W. and Yoon, S.-C.: Seasonal characteristics of chemically
 828 apportioned aerosol optical properties at Seoul and Gosan, Korea, Atmos. Environ., 43(6),
 829 1320–1328, doi:10.1016/j.atmosenv.2008.11.044, 2009.

830 Lee, Y. H., Choi, Y. and Ghim, Y. S.: Classification of diurnal patterns of particulate
 831 inorganic ions downwind of metropolitan Seoul, in submission, 2015.

832 Lelieveld, J., Butler, T. M., Crowley, J. N., Dillon, T. J., Fischer, H., Ganzeveld, L., Harder,
 833 H., Lawrence, M. G., Martinez, M., Taraborrelli, D. and Williams, J.: Atmospheric oxidation
 834 capacity sustained by a tropical forest, Nature, 452(7188), 737–740, doi:10.1038/nature06870,
 835 2008.

836 Levy, R. C., Remer, L. A., Mattoo, S., Vermote, E. F. and Kaufman, Y. J.: Second-generation
 837 operational algorithm: Retrieval of aerosol properties over land from inversion of Moderate
 838 Resolution Imaging Spectroradiometer spectral reflectance: NEW MODIS RETRIEVAL OF
 839 AEROSOL OVER LAND, J. Geophys. Res. Atmospheres, 112(D13), D13211,
 840 doi:10.1029/2006JD007811, 2007.

841 Liu, Z., Liu, Q., Lin, H.-C., Schwartz, C. S., Lee, Y.-H. and Wang, T.: Three-dimensional
 842 variational assimilation of MODIS aerosol optical depth: Implementation and application to a

843 dust storm over East Asia, *J. Geophys. Res. Atmospheres*, 116(D23), D23206,
 844 doi:10.1029/2011JD016159, 2011.

845 Lu, Z., Streets, D. G., Zhang, Q., Wang, S., Carmichael, G. R., Cheng, Y. F., Wei, C., Chin,
 846 M., Diehl, T. and Tan, Q.: Sulfur dioxide emissions in China and sulfur trends in East Asia
 847 since 2000, *Atmos. Chem. Phys.*, 10(13), 6311–6331, doi:10.5194/acp-10-6311-2010, 2010.

848 Malm, W. C. and Hand, J. L.: An examination of the physical and optical properties of
 849 aerosols collected in the IMPROVE program, *Atmos. Environ.*, 41(16), 3407–3427,
 850 doi:10.1016/j.atmosenv.2006.12.012, 2007.

851 Martin, R. V., Jacob, D. J., Yantosca, R. M., Chin, M. and Ginoux, P.: Global and regional
 852 decreases in tropospheric oxidants from photochemical effects of aerosols, *J. Geophys. Res.*
 853 *Atmospheres*, 108(D3), 4097, doi:10.1029/2002JD002622, 2003.

854 Matsui, H., Koike, M., Kondo, Y., Takami, A., Fast, J. D., Kanaya, Y. and Takigawa, M.:
 855 Volatility basis-set approach simulation of organic aerosol formation in East Asia:
 856 implications for anthropogenic–biogenic interaction and controllable amounts, *Atmos. Chem.*
 857 *Phys.*, 14(18), 9513–9535, doi:10.5194/acp-14-9513-2014, 2014.

858 Munchak, L. A., Levy, R. C., Mattoo, S., Remer, L. A., Holben, B. N., Schafer, J. S.,
 859 Hostetler, C. A. and Ferrare, R. A.: MODIS 3 km aerosol product: applications over land in
 860 an urban/suburban region, *Atmos. Meas. Tech.*, 6(7), 1747–1759, doi:10.5194/amt-6-1747-
 861 2013, 2013.

862 Myneni, R. B., Hoffman, S., Knyazikhin, Y., Privette, J. L., Glassy, J., Tian, Y., Wang, Y.,
 863 Song, X., Zhang, Y., Smith, G. R., Lotsch, A., Friedl, M., Morisette, J. T., Votava, P., Nemani,
 864 R. R. and Running, S. W.: Global products of vegetation leaf area and fraction absorbed PAR
 865 from year one of MODIS data, *Remote Sens. Environ.*, 83(1–2), 214–231,
 866 doi:10.1016/S0034-4257(02)00074-3, 2002.

867 NCL: The NCAR Command Language (Version 6.2.1) [Software], Boulder Colo.
 868 UCARNCARCISLVETS, doi:10.5065/D6WD3XH5, 2014.

869 Otte, T. L. and Pleim, J. E.: The Meteorology-Chemistry Interface Processor (MCIP) for the
 870 CMAQ modeling system: updates through MCIPv3.4.1, *Geosci. Model Dev.*, 3(1), 243–256,
 871 doi:10.5194/gmd-3-243-2010, 2010.

872 Park, M. E., Song, C. H., Park, R. S., Lee, J., Kim, J., Lee, S., Woo, J.-H., Carmichael, G. R.,
 873 Eck, T. F., Holben, B. N., Lee, S.-S., Song, C. K. and Hong, Y. D.: New approach to monitor
 874 transboundary particulate pollution over Northeast Asia, *Atmos. Chem. Phys.*, 14(2), 659–674,
 875 doi:10.5194/acp-14-659-2014, 2014a.

876 Park, R. S., Song, C. H., Han, K. M., Park, M. E., Lee, S.-S., Kim, S.-B. and Shimizu, A.: A
 877 study on the aerosol optical properties over East Asia using a combination of CMAQ-
 878 simulated aerosol optical properties and remote-sensing data via a data assimilation technique,
 879 *Atmos. Chem. Phys.*, 11(23), 12275–12296, doi:10.5194/acp-11-12275-2011, 2011.

880 Park, R. S., Lee, S., Shin, S.-K. and Song, C. H.: Contribution of ammonium nitrate to aerosol
 881 optical depth and direct radiative forcing by aerosols over East Asia, *Atmos. Chem. Phys.*,
 882 14(4), 2185–2201, doi:10.5194/acp-14-2185-2014, 2014b.

883 Pebesma, E.: spacetime: Spatio-Temporal Data in R, *J. Stat. Softw.*, 51(7) [online] Available
 884 from: <http://www.jstatsoft.org/v51/i07>, 2012.

885 Pebesma, E. J.: Multivariable geostatistics in S: the gstat package, *Comput. Geosci.*, 30(7),
 886 683–691, doi:10.1016/j.cageo.2004.03.012, 2004.

887 Pope, C. A. and Dockery, D. W.: Health Effects of Fine Particulate Air Pollution: Lines that
 888 Connect, *J. Air Amp Waste Manag. Assoc.*, 56(6), 709–742,
 889 doi:10.1080/10473289.2006.10464485, 2006.

890 R Development Core Team: R: A Language and Environment for Statistical Computing, R
 891 Foundation for Statistical Computing, Vienna, Austria. [online] Available from:
 892 <http://www.R-project.org/>, 2011.

893 Reff, A., Bhave, P. V., Simon, H., Pace, T. G., Pouliot, G. A., Mobley, J. D. and Houyoux,
 894 M.: Emissions Inventory of PM_{2.5} Trace Elements across the United States, *Environ. Sci.*
 895 *Technol.*, 43(15), 5790–5796, doi:10.1021/es802930x, 2009.

896 Remer, L. A., Kaufman, Y. J., Tanré, D., Mattoo, S., Chu, D. A., Martins, J. V., Li, R.-R.,
 897 Ichoku, C., Levy, R. C., Kleidman, R. G., Eck, T. F., Vermote, E. and Holben, B. N.: The
 898 MODIS Aerosol Algorithm, Products, and Validation, *J. Atmospheric Sci.*, 62(4), 947–973,
 899 doi:10.1175/JAS3385.1, 2005.

900 Al-Saadi, J., Szykman, J., Pierce, R. B., Kittaka, C., Neil, D., Chu, D. A., Remer, L., Gumley,
 901 L., Prins, E., Weinstock, L., MacDonald, C., Wayland, R., Dimmick, F. and Fishman, J.:

902 Improving National Air Quality Forecasts with Satellite Aerosol Observations, *Bull. Am.*
903 *Meteorol. Soc.*, 86(9), 1249–1261, doi:10.1175/BAMS-86-9-1249, 2005.

904 Saide, P. E., Carmichael, G. R., Liu, Z., Schwartz, C. S., Lin, H. C., da Silva, A. M. and Hyer,
905 E.: Aerosol optical depth assimilation for a size-resolved sectional model: impacts of
906 observationally constrained, multi-wavelength and fine mode retrievals on regional scale
907 analyses and forecasts, *Atmos. Chem. Phys.*, 13(20), 10425–10444, doi:10.5194/acp-13-
908 10425-2013, 2013.

909 Sakulyanontvittaya, T., Duhl, T., Wiedinmyer, C., Helmig, D., Matsunaga, S., Potosnak, M.,
910 Milford, J. and Guenther, A.: Monoterpene and Sesquiterpene Emission Estimates for the
911 United States, *Environ. Sci. Technol.*, 42(5), 1623–1629, doi:10.1021/es702274e, 2008.

912 Savage, N. H., Agnew, P., Davis, L. S., Ordóñez, C., Thorpe, R., Johnson, C. E., O'Connor, F.
913 M. and Dalvi, M.: Air quality modelling using the Met Office Unified Model (AQUUM OS24-
914 26): model description and initial evaluation, *Geosci. Model Dev.*, 6(2), 353–372,
915 doi:10.5194/gmd-6-353-2013, 2013.

916 Saxena, P., Belle Hudischewskyj, A., Seigneur, C. and Seinfeld, J. H.: A comparative study of
917 equilibrium approaches to the chemical characterization of secondary aerosols, *Atmos.*
918 *Environ.* 1967, 20(7), 1471–1483, doi:10.1016/0004-6981(86)90019-3, 1986.

919 Schwartz, C. S., Liu, Z., Lin, H.-C. and McKeen, S. A.: Simultaneous three-dimensional
920 variational assimilation of surface fine particulate matter and MODIS aerosol optical depth, *J.*
921 *Geophys. Res. Atmospheres*, 117(D13), D13202, doi:10.1029/2011JD017383, 2012.

922 Seinfeld, J. H. and Pandis, S. N.: *Atmospheric chemistry and physics: from air pollution to*
923 *climate change*, John Wiley & Sons., 2012.

924 Shi, Y., Zhang, J., Reid, J. S., Holben, B., Hyer, E. J. and Curtis, C.: An analysis of the
925 collection 5 MODIS over-ocean aerosol optical depth product for its implication in aerosol
926 assimilation, *Atmos. Chem. Phys.*, 11(2), 557–565, doi:10.5194/acp-11-557-2011, 2011.

927 Skamarock, W. C. and Klemp, J. B.: A time-split nonhydrostatic atmospheric model for
928 weather research and forecasting applications, *J. Comput. Phys.*, 227(7), 3465–3485,
929 doi:10.1016/j.jcp.2007.01.037, 2008.

930 Slowik, J. G., Stroud, C., Bottenheim, J. W., Brickell, P. C., Chang, R. Y.-W., Liggio, J.,
931 Makar, P. A., Martin, R. V., Moran, M. D., Shantz, N. C., Sjostedt, S. J., van Donkelaar, A.,

932 Vlasenko, A., Wiebe, H. A., Xia, A. G., Zhang, J., Leaitch, W. R. and Abbatt, J. P. D.:
 933 Characterization of a large biogenic secondary organic aerosol event from eastern Canadian
 934 forests, *Atmos. Chem. Phys.*, 10(6), 2825–2845, doi:10.5194/acp-10-2825-2010, 2010.

935 Smith, S. J., van Aardenne, J., Klimont, Z., Andres, R. J., Volke, A. and Delgado Arias, S.:
 936 Anthropogenic sulfur dioxide emissions: 1850–2005, *Atmos. Chem. Phys.*, 11(3), 1101–1116,
 937 doi:10.5194/acp-11-1101-2011, 2011.

938 Song, C. H. and Carmichael, G. R.: The aging process of naturally emitted aerosol (sea-salt
 939 and mineral aerosol) during long range transport, *Atmos. Environ.*, 33(14), 2203–2218,
 940 doi:10.1016/S1352-2310(98)00301-X, 1999.

941 Song, C. H. and Carmichael, G. R.: Gas-Particle Partitioning of Nitric Acid Modulated by
 942 Alkaline Aerosol, *J. Atmospheric Chem.*, 40(1), 1–22, 2001.

943 Song, C. H., Chen, G., Hanna, S. R., Crawford, J. and Davis, D. D.: Dispersion and chemical
 944 evolution of ship plumes in the marine boundary layer: Investigation of O₃/NO_y/HO_x
 945 chemistry, *J. Geophys. Res. Atmospheres*, 108(D4), 4143, doi:10.1029/2002JD002216, 2003.

946 Song, C. H., Park, M. E., Lee, K. H., Ahn, H. J., Lee, Y., Kim, J. Y., Han, K. M., Kim, J.,
 947 Ghim, Y. S. and Kim, Y. J.: An investigation into seasonal and regional aerosol
 948 characteristics in East Asia using model-predicted and remotely-sensed aerosol properties,
 949 *Atmos. Chem. Phys.*, 8(22), 6627–6654, doi:10.5194/acp-8-6627-2008, 2008.

950 Song, C. H., Kim, H. S., von Glasow, R., Brimblecombe, P., Kim, J., Park, R. J., Woo, J. H.
 951 and Kim, Y. H.: Source identification and budget analysis on elevated levels of formaldehyde
 952 within the ship plumes: a ship-plume photochemical/dynamic model analysis, *Atmos. Chem.*
 953 *Phys.*, 10(23), 11969–11985, doi:10.5194/acp-10-11969-2010, 2010.

954 Sörgel, M., Regelin, E., Bozem, H., Diesch, J.-M., Drewnick, F., Fischer, H., Harder, H., Held,
 955 A., Hosaynali-Beygi, Z., Martinez, M. and Zetzsch, C.: Quantification of the unknown
 956 HONO daytime source and its relation to NO₂, *Atmos. Chem. Phys.*, 11(20), 10433–10447,
 957 doi:10.5194/acp-11-10433-2011, 2011.

958 Stelson, A. W., Bassett, M. E. and Seinfeld, J. H.: Thermodynamic equilibrium properties of
 959 aqueous solutions of nitrate, sulfate and ammonium., *ACID PRECIP SER* 1984, 1984.

960 Stemmler, K., Ammann, M., Donders, C., Kleffmann, J. and George, C.: Photosensitized
 961 reduction of nitrogen dioxide on humic acid as a source of nitrous acid, *Nature*, 440(7081),
 962 195–198, doi:10.1038/nature04603, 2006.

963 Tsimpidi, A. P., Karydis, V. A., Zavala, M., Lei, W., Molina, L., Ulbrich, I. M., Jimenez, J. L.
 964 and Pandis, S. N.: Evaluation of the volatility basis-set approach for the simulation of organic
 965 aerosol formation in the Mexico City metropolitan area, *Atmos. Chem. Phys.*, 10(2), 525–546,
 966 doi:10.5194/acp-10-525-2010, 2010.

967 Wiedinmyer, C., Akagi, S. K., Yokelson, R. J., Emmons, L. K., Al-Saadi, J. A., Orlando, J. J.
 968 and Soja, A. J.: The Fire INventory from NCAR (FINN): a high resolution global model to
 969 estimate the emissions from open burning, *Geosci. Model Dev.*, 4(3), 625–641,
 970 doi:10.5194/gmd-4-625-2011, 2011.

971 Willmott, C. and Matsuura, K.: Advantages of the mean absolute error (MAE) over the root
 972 mean square error (RMSE) in assessing average model performance, *Clim. Res.*, 30, 79–82,
 973 doi:10.3354/cr030079, 2005.

974 Willmott, C. J.: On the Validation of Models, *Phys. Geogr.*, 2(2), 184–194,
 975 doi:10.1080/02723646.1981.10642213, 1981.

976 Willmott, C. J., Matsuura, K. and Robeson, S. M.: Ambiguities inherent in sums-of-squares-
 977 based error statistics, *Atmos. Environ.*, 43(3), 749–752, doi:10.1016/j.atmosenv.2008.10.005,
 978 2009.

979 Woo, J.-H., Choi, K.-C., Kim, H. K., Baek, B. H., Jang, M., Eum, J.-H., Song, C. H., Ma, Y.-
 980 I., Sunwoo, Y., Chang, L.-S. and Yoo, S. H.: Development of an anthropogenic emissions
 981 processing system for Asia using SMOKE, *Atmos. Environ.*, 58, 5–13,
 982 doi:10.1016/j.atmosenv.2011.10.042, 2012.

983 Wyatt Appel, K., Bhawe, P. V., Gilliland, A. B., Sarwar, G. and Roselle, S. J.: Evaluation of
 984 the community multiscale air quality (CMAQ) model version 4.5: Sensitivities impacting
 985 model performance; Part II—particulate matter, *Atmos. Environ.*, 42(24), 6057–6066,
 986 doi:10.1016/j.atmosenv.2008.03.036, 2008.

987 Zhang, Q., Jimenez, J. L., Canagaratna, M. R., Allan, J. D., Coe, H., Ulbrich, I., Alfarra, M.
 988 R., Takami, A., Middlebrook, A. M., Sun, Y. L., Dzepina, K., Dunlea, E., Docherty, K.,
 989 DeCarlo, P. F., Salcedo, D., Onasch, T., Jayne, J. T., Miyoshi, T., Shimono, A., Hatakeyama,

990 S., Takegawa, N., Kondo, Y., Schneider, J., Drewnick, F., Borrmann, S., Weimer, S.,
 991 Demerjian, K., Williams, P., Bower, K., Bahreini, R., Cottrell, L., Griffin, R. J., Rautiainen, J.,
 992 Sun, J. Y., Zhang, Y. M. and Worsnop, D. R.: Ubiquity and dominance of oxygenated species
 993 in organic aerosols in anthropogenically-influenced Northern Hemisphere midlatitudes,
 994 *Geophys. Res. Lett.*, 34(13), L13801, doi:10.1029/2007GL029979, 2007.

995 Zhang, X. Y., Wang, Y. Q., Niu, T., Zhang, X. C., Gong, S. L., Zhang, Y. M. and Sun, J. Y.:
 996 Atmospheric aerosol compositions in China: spatial/temporal variability, chemical signature,
 997 regional haze distribution and comparisons with global aerosols, *Atmos. Chem. Phys.*, 12(2),
 998 779–799, doi:10.5194/acp-12-779-2012, 2012.

999 Zhou, X., Zhang, N., TerAvest, M., Tang, D., Hou, J., Bertman, S., Alaghmand, M., Shepson,
 1000 P. B., Carroll, M. A., Griffith, S., Dusanter, S. and Stevens, P. S.: Nitric acid photolysis on
 1001 forest canopy surface as a source for tropospheric nitrous acid, *Nat. Geosci.*, 4(7), 440–443,
 1002 doi:10.1038/ngeo1164, 2011.

1003 Zoogman, P., Jacob, D. J., Chance, K., Liu, X., Lin, M., Fiore, A. and Travis, K.: Monitoring
 1004 high-ozone events in the US Intermountain West using TEMPO geostationary satellite
 1005 observations, *Atmos. Chem. Phys.*, 14(12), 6261–6271, doi:10.5194/acp-14-6261-2014, 2014.

1006

Table 1. WRF and CMAQ model configurations.

| WRF (ver. 3.5.1) | | CMAQ (ver. 5.0.1) | |
|--------------------------------|---|--------------------|---------------------------------------|
| Microphysics scheme | WRF single-moment 3 class | Chemical mechanism | SAPRC-99 |
| Long- and short-wave radiation | Rapid Radiation Transfer Model for GCMs (RRTMG) | Aerosol module | AERO-6 |
| Planetary boundary layer | Yonsei University scheme | Chemistry solver | Euler backward iterative (EBI) solver |
| Land-surface model | Noah-MP | Photolysis module | In-line photolysis calculations |

Table 2. Values used in observation operators for estimating aerosol optical properties (AOPs).

| Method for estimating aerosol optical properties | Aerosol speciation | Hygroscopic aerosols | α_{OC}^1 | α_{BC}^2 | α_{SSAM}^3 | α_{SSCM}^4 |
|--|---|--|-----------------|-----------------|-------------------|-------------------|
| Chin et al. (2002) | (NH ₄) ₂ SO ₄ , OC, BC, dust (7 size bins), sea-salt (2 modes) | (NH ₄) ₂ SO ₄ , OC, BC, sea-salt | 2.67 | 9.28 | 1.15 | 0.13 |
| Martin et al. (2003) | (NH ₄) ₂ SO ₄ , OC, BC, dust (7 size bins), sea-salt (2 modes) | (NH ₄) ₂ SO ₄ , OC, BC, sea-salt | 2.82 | 8.05 | 2.37 | 0.94 |
| Malm and Hand (2007) | NH ₄ NO ₃ , (NH ₄) ₂ SO ₄ , organic matter, soil, coarse mass, sea-salt | NH ₄ NO ₃ , (NH ₄) ₂ SO ₄ , sea-salt | 4.00 | 10.00 | 1.37 | 1.37 |

Dry mass extinction efficiencies (m² g⁻¹) at 550nm of ¹ OC, ² BC, ³ sea-salt in accumulation mode and ⁴ sea-salt in coarse mode

Note: In cases of Chin et al. (2002) and Martin et al. (2003), the AOPs for sulfate were used for calculating AOPs for NH₄NO₃ and (NH₄)₂SO₄.

Table 3. Definition of model configurations.

| Configuration | Observation operator | Control variable |
|---------------|----------------------|---|
| A1 | Chin et al. (2002) | Total aerosol mass concentration |
| A2 | | SO_4^{2-} mass concentration |
| A3 | | SO_4^{2-} and OAs mass concentration |
| A4 | | SO_4^{2-} , NO_3^- , NH_4^+ and OAs mass concentration |
| B1 | Martin et al. (2003) | Total aerosol mass concentration |
| B2 | | SO_4^{2-} mass concentration |
| B3 | | SO_4^{2-} and OAs mass concentration |
| B4 | | SO_4^{2-} , NO_3^- , NH_4^+ and OAs mass concentration |
| C1 | Malm and Hand (2007) | Total aerosol mass concentration |
| C2 | | SO_4^{2-} mass concentration |
| C3 | | SO_4^{2-} and OAs mass concentration |
| C4 | | SO_4^{2-} , NO_3^- , NH_4^+ and OAs mass concentration |

Table 4. Performance metrics for AOD and PM₁₀ hindcasts on the ten selected episodes at six AERONET sites and nearby NAMIS PM₁₀ stations in SMA.

| Configuration | AOD (N ¹ = 277) | | | | | | | | PM ₁₀ (N = 340) | | | | | | | |
|---------------|----------------------------|------------------|------------------|----------------|-------------------|-----------------|------------------|------------------|----------------------------|------|-------|------|--------------------|------------------|------|-------|
| | IOA ² | MFE ³ | MFB ⁴ | R ⁵ | RMSE ⁶ | MB ⁷ | MNE ⁸ | MNB ⁹ | IOA | MFE | MFB | R | RMSE ¹⁰ | MB ¹⁰ | MNE | MNB |
| noSTK | 0.48 | 113.2 | -113.2 | 0.61 | 0.60 | -0.53 | 70.0 | -70.0 | 0.47 | 89.0 | -88.5 | 0.54 | 55.15 | -48.40 | 58.9 | -58.4 |
| A1 | 0.62 | 37.4 | -22.1 | 0.46 | 0.36 | -0.16 | 32.5 | -13.7 | 0.60 | 35.4 | -22.7 | 0.44 | 36.07 | -15.80 | 31.1 | -14.7 |
| A2 | 0.60 | 39.8 | -20.9 | 0.41 | 0.37 | -0.15 | 35.8 | -11.3 | 0.58 | 39.4 | -34.7 | 0.50 | 37.13 | -24.65 | 31.6 | -25.8 |
| A3 | 0.63 | 38.7 | -22.5 | 0.46 | 0.36 | -0.16 | 34.0 | -13.5 | 0.64 | 33.0 | -23.1 | 0.52 | 33.15 | -17.07 | 28.4 | -16.2 |
| A4 | 0.63 | 37.4 | -22.0 | 0.47 | 0.35 | -0.16 | 32.6 | -13.5 | 0.64 | 36.2 | -28.3 | 0.53 | 34.58 | -19.79 | 30.3 | -20.4 |
| B1 | 0.54 | 43.1 | -27.1 | 0.33 | 0.40 | -0.18 | 36.4 | -16.2 | 0.53 | 41.1 | -30.0 | 0.31 | 40.01 | -20.90 | 33.9 | -20.0 |
| B2 | 0.51 | 44.7 | -25.2 | 0.27 | 0.41 | -0.17 | 39.5 | -13.3 | 0.53 | 43.8 | -39.2 | 0.37 | 40.94 | -27.50 | 34.1 | -28.5 |
| B3 | 0.56 | 42.3 | -25.8 | 0.35 | 0.39 | -0.18 | 36.6 | -15.2 | 0.56 | 38.0 | -29.6 | 0.39 | 37.43 | -21.65 | 31.2 | -21.0 |
| B4 | 0.55 | 41.9 | -24.7 | 0.34 | 0.39 | -0.17 | 36.3 | -14.2 | 0.56 | 40.7 | -33.9 | 0.42 | 38.30 | -23.84 | 32.8 | -24.4 |
| C1 | 0.50 | 44.4 | -37.5 | 0.28 | 0.43 | -0.26 | 34.3 | -26.3 | 0.55 | 35.8 | -14.5 | 0.32 | 38.41 | -9.82 | 33.4 | -5.4 |
| C2 | 0.47 | 45.7 | -34.2 | 0.20 | 0.43 | -0.24 | 36.7 | -22.7 | 0.55 | 36.3 | -26.0 | 0.37 | 36.86 | -19.43 | 30.3 | -17.6 |
| C3 | 0.53 | 41.7 | -30.5 | 0.34 | 0.40 | -0.22 | 34.1 | -20.5 | 0.60 | 32.9 | -19.6 | 0.44 | 34.07 | -14.92 | 29.1 | -12.5 |
| C4 | 0.53 | 41.7 | -32.4 | 0.35 | 0.41 | -0.23 | 32.4 | -22.6 | 0.61 | 34.8 | -21.8 | 0.44 | 34.78 | -15.68 | 30.4 | -14.0 |

¹ the number of paired data, ² index of agreement, ³ mean fractional error, ⁴ mean fractional bias, ⁵ Pearson product-moment correlation coefficient, ⁶ root mean square error, ⁷ mean bias, ⁸ mean normalized error, and ⁹ mean normalized bias. The units of all of metrics are dimensionless except ¹⁰ for $\mu\text{g m}^{-3}$.

Table 5. Performance metrics for PM₁₀ hindcasting on the ten selected episodes at 58 NAMIS PM₁₀ stations in SMA. Abbreviations are the same as those in Table 3.

| Configuration | H+1 to H+6 (N = 4823) | | | | | | | | H+7 to H+12 (N = 4921) | | | | | | | |
|---------------|-----------------------|------|-------|------|-------|--------|------|-------|------------------------|------|-------|------|-------|--------|------|-------|
| | IOA | MFE | MFB | R | RMSE | MB | MNE | MNB | IOA | MFE | MFB | R | RMSE | MB | MNE | MNB |
| noSTK | 0.45 | 99.6 | -98.7 | 0.44 | 62.98 | -54.59 | 63.9 | -62.6 | 0.55 | 64.7 | -36.9 | 0.30 | 56.76 | -17.77 | 56.5 | -12.9 |
| A1 | 0.62 | 42.2 | -30.9 | 0.47 | 40.64 | -21.41 | 35.6 | -19.7 | 0.62 | 43.9 | 1.5 | 0.37 | 49.17 | 5.27 | 51.2 | 19.1 |
| A2 | 0.57 | 49.1 | -43.4 | 0.48 | 43.81 | -30.49 | 38.5 | -30.4 | 0.60 | 45.1 | -4.0 | 0.34 | 49.81 | 0.60 | 49.9 | 13.1 |
| A3 | 0.64 | 40.5 | -30.4 | 0.50 | 39.46 | -21.83 | 34.2 | -20.1 | 0.63 | 43.5 | 5.8 | 0.39 | 50.51 | 9.17 | 52.7 | 23.9 |
| A4 | 0.63 | 44.6 | -36.3 | 0.52 | 40.70 | -24.99 | 36.3 | -24.7 | 0.62 | 43.6 | 1.2 | 0.38 | 49.44 | 5.10 | 50.6 | 18.5 |
| B1 | 0.54 | 48.8 | -39.6 | 0.35 | 45.12 | -27.64 | 38.8 | -26.1 | 0.58 | 46.0 | -3.6 | 0.31 | 49.18 | 0.71 | 50.8 | 14.1 |
| B2 | 0.51 | 53.9 | -48.9 | 0.36 | 47.76 | -34.14 | 41.0 | -33.9 | 0.59 | 46.3 | -7.4 | 0.33 | 48.73 | -2.37 | 49.1 | 9.3 |
| B3 | 0.56 | 45.9 | -37.9 | 0.40 | 43.36 | -27.48 | 36.9 | -25.8 | 0.61 | 44.6 | 0.7 | 0.35 | 48.81 | 4.07 | 51.0 | 17.9 |
| A4 | 0.56 | 49.7 | -43.0 | 0.43 | 44.46 | -30.05 | 38.9 | -29.6 | 0.60 | 45.2 | -3.1 | 0.34 | 48.87 | 1.07 | 50.0 | 14.0 |
| C1 | 0.60 | 40.4 | -22.7 | 0.39 | 40.82 | -15.98 | 35.9 | -11.7 | 0.58 | 45.9 | 6.6 | 0.32 | 51.68 | 9.84 | 56.0 | 26.5 |
| C2 | 0.56 | 43.7 | -34.3 | 0.40 | 42.22 | -25.43 | 35.6 | -22.9 | 0.58 | 45.9 | 2.0 | 0.31 | 51.37 | 5.63 | 53.6 | 20.7 |
| C3 | 0.63 | 39.0 | -27.3 | 0.47 | 39.00 | -20.13 | 33.3 | -17.5 | 0.61 | 44.1 | 7.3 | 0.37 | 51.46 | 10.64 | 54.3 | 26.3 |
| C4 | 0.63 | 41.2 | -29.9 | 0.48 | 39.45 | -21.30 | 34.5 | -19.4 | 0.61 | 44.2 | 4.7 | 0.36 | 50.69 | 8.29 | 53.2 | 23.2 |

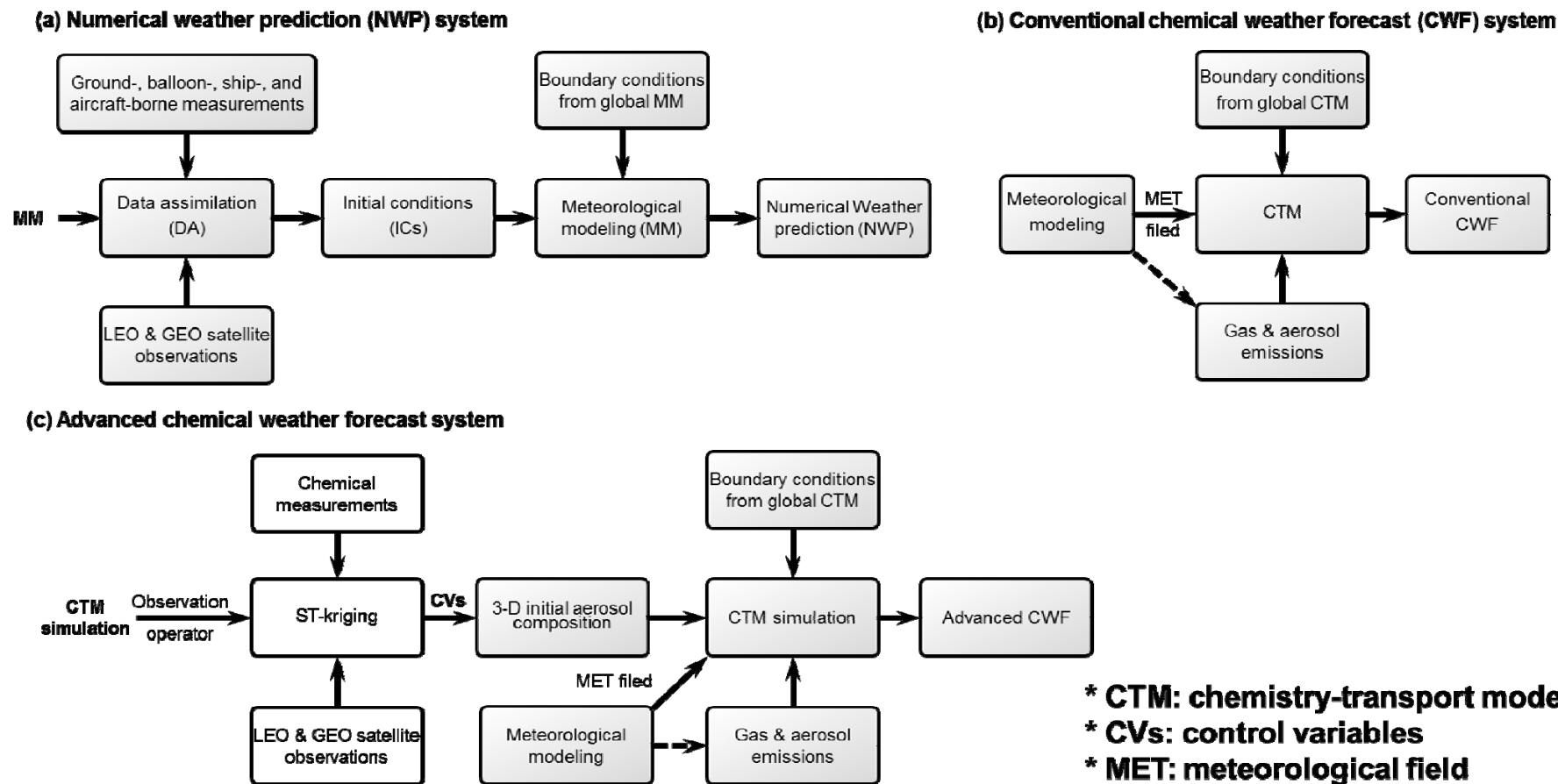


Figure 1. General structure of a) numerical weather prediction (NWP), b) conventional chemical weather forecast (CWF), and c) advanced chemical weather forecast system.

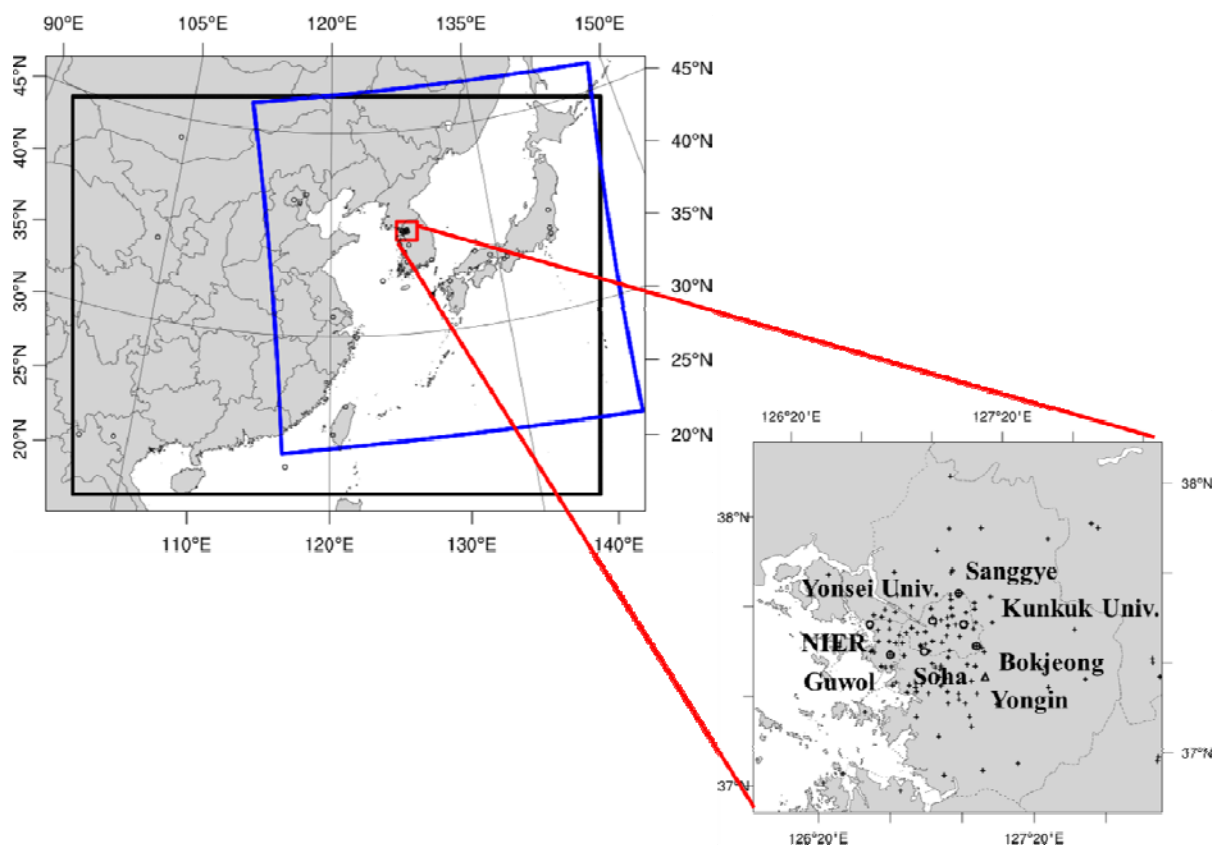


Figure 2. Domains of CMAQ model simulations (black), GOCI sensor coverage (blue), and Seoul Metropolitan area (red). Also shown are seven AERONET level-2 sites (circles), 58 NAMIS PM_{10} sites (crosses), and a PM composition observation site (triangle) in greater Seoul area, respectively.

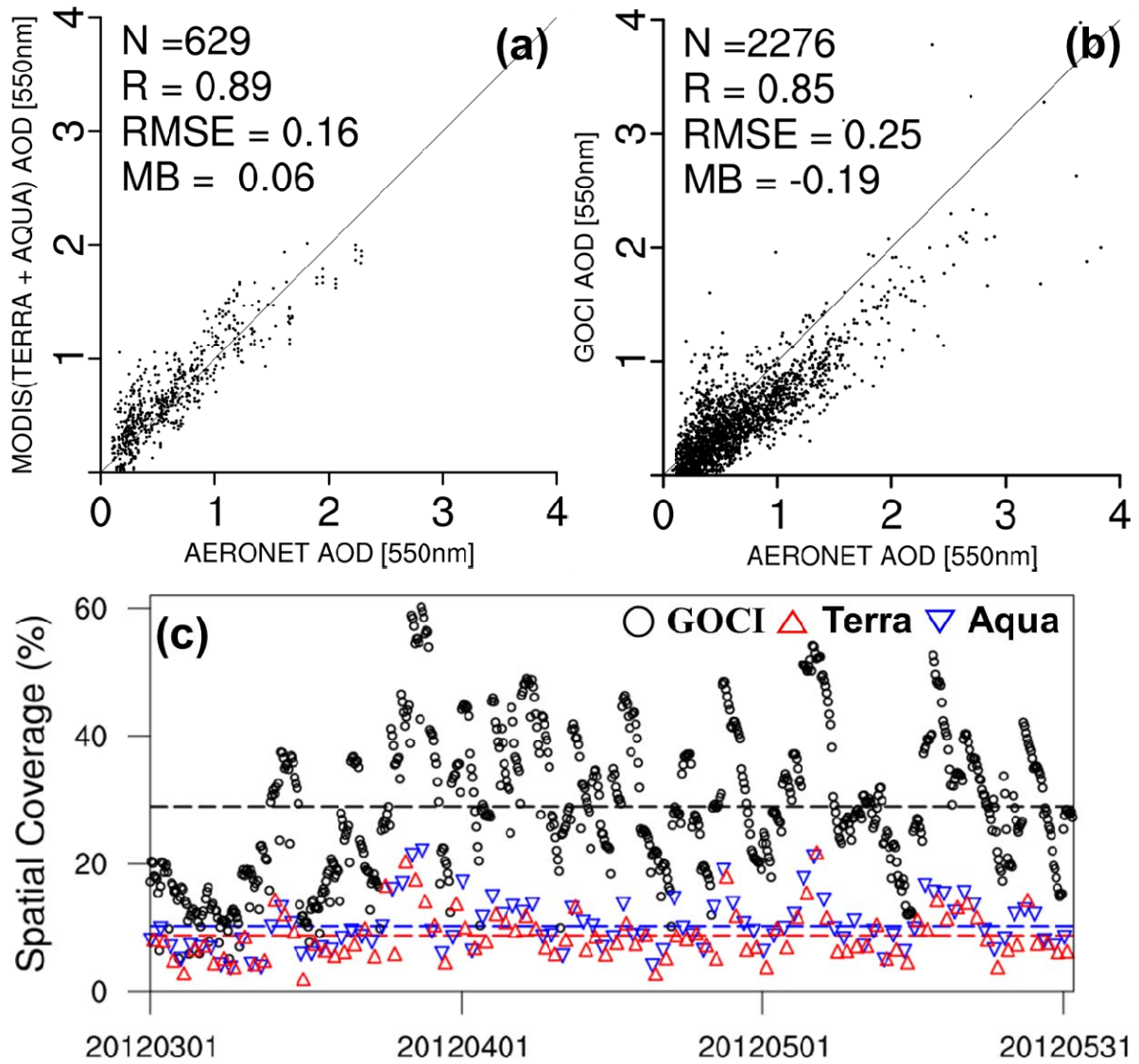


Figure 3. Scatter plots of (a) Aqua/Terra MODIS AODs vs. AERONET level-2 AODs and (b) GOCI AODs vs. AERONET level-2 AODs at 550 nm during the DRAGON campaign over the GOCI domain. N , R , $RMSE$, and MB represent the number of observations, the regression coefficient, root mean square error, and mean bias, respectively. Hourly-resolved Aqua/Terra MODIS and GOCI spatial coverages (%) are also shown in the panel (c) from 1 March to 31 May, 2012.

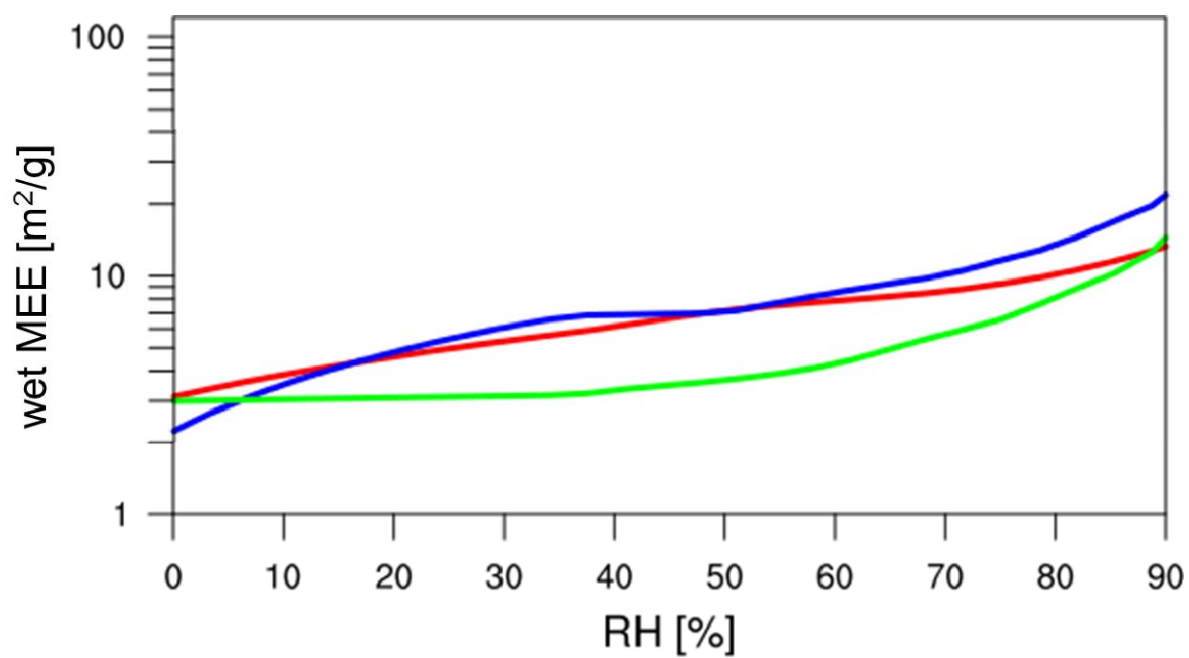


Figure 4. Mass extinction efficiencies (MEEs) calculated for SO_4^{2-} , NO_3^- , and NH_4^+ at a wavelength of 550 nm as a function of relative humidity (%) from three observation operators.

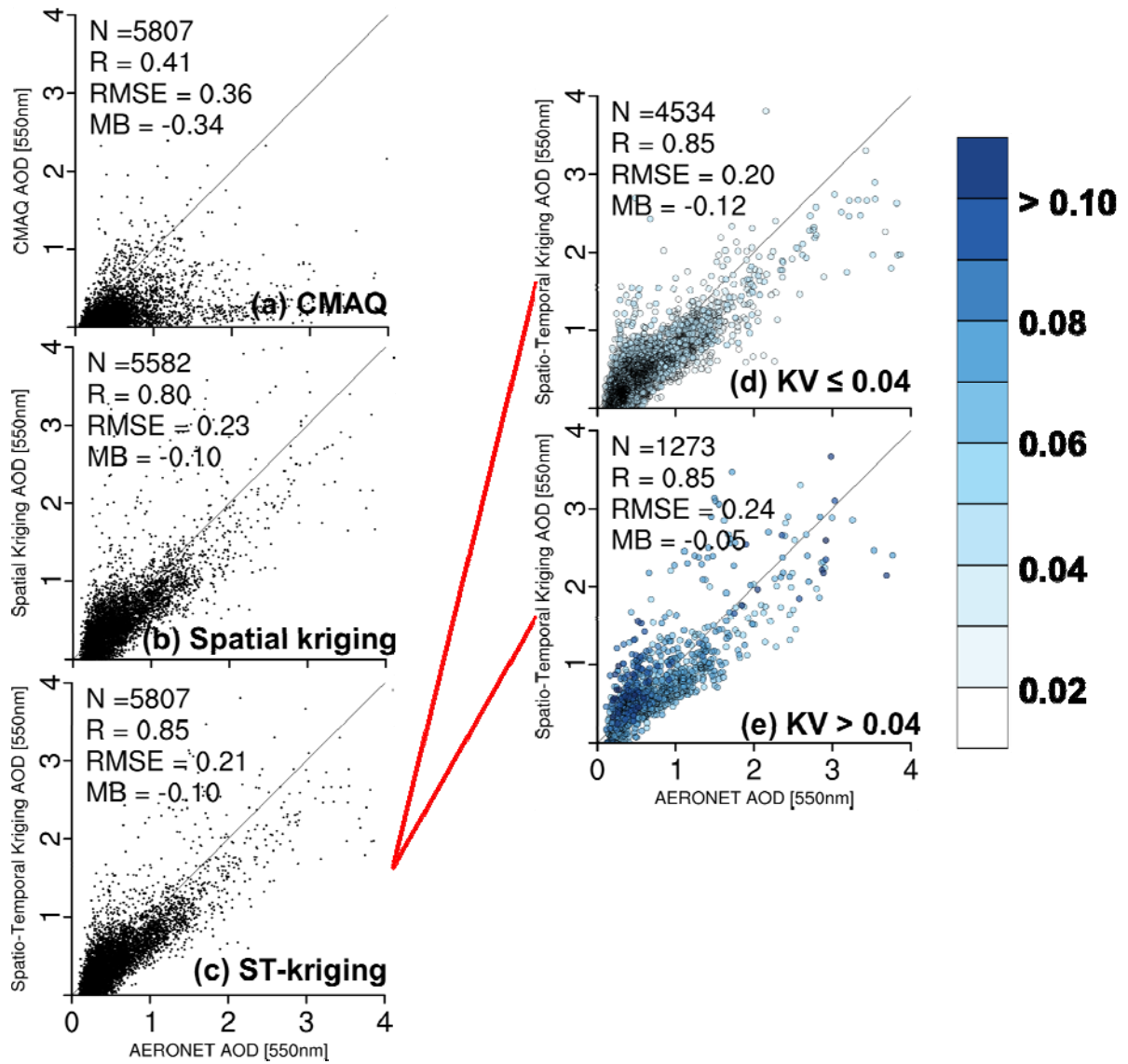


Figure 5. Scatter plots of (a) background CMAQ model AODs, (b) spatial kriging AODs, and (c) ST-kriging AODs vs. AERONET level-2 AODs at 550 nm. Plots of ST-kriging with kriging variances (KVs) less equal 0.04 (d) and larger than 0.04 (e) are also shown. The color scale shown in Fig. 5 (e) presents the KVs of ST-kriging AODs. The number of AOD in (b) is smaller than those of (a) and (c) due to the missing hourly AOD fields by the anomaly in GOCI.

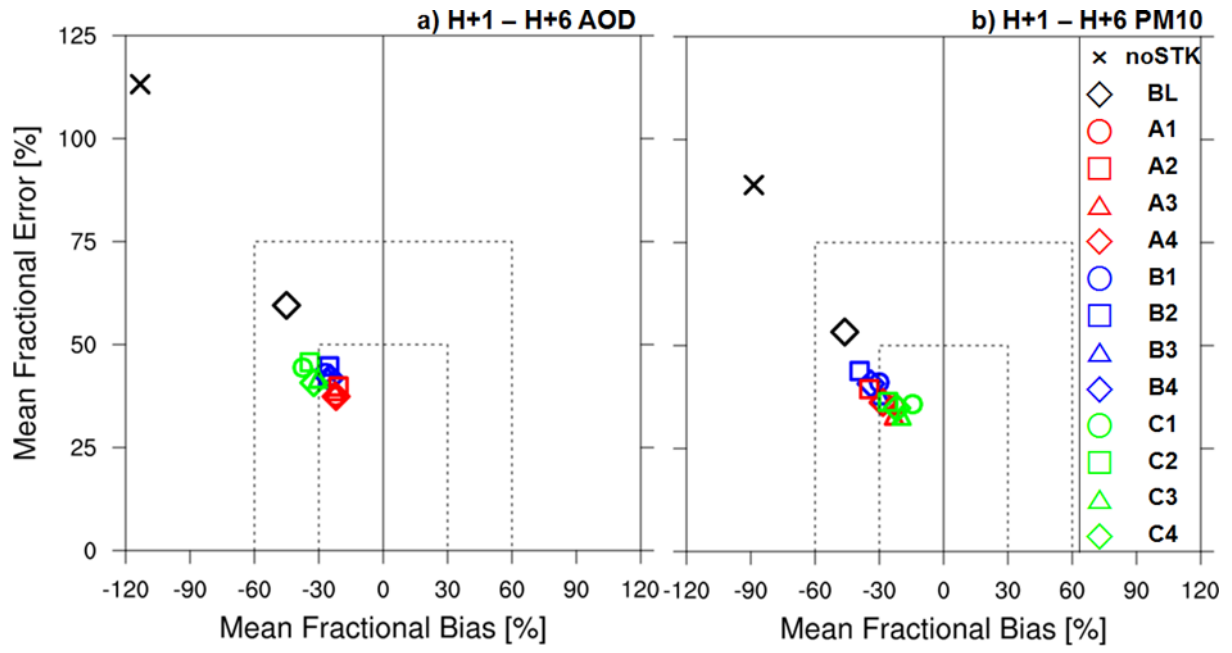


Figure 6. Soccer plot analysis for AOD (left panel) and PM_{10} (right panel) data from the first 6-h observations and the model data at six selected sites. BL (denoted by black diamond) represents the case of bilinear interpolation method discussed in Sect. 3. 2.

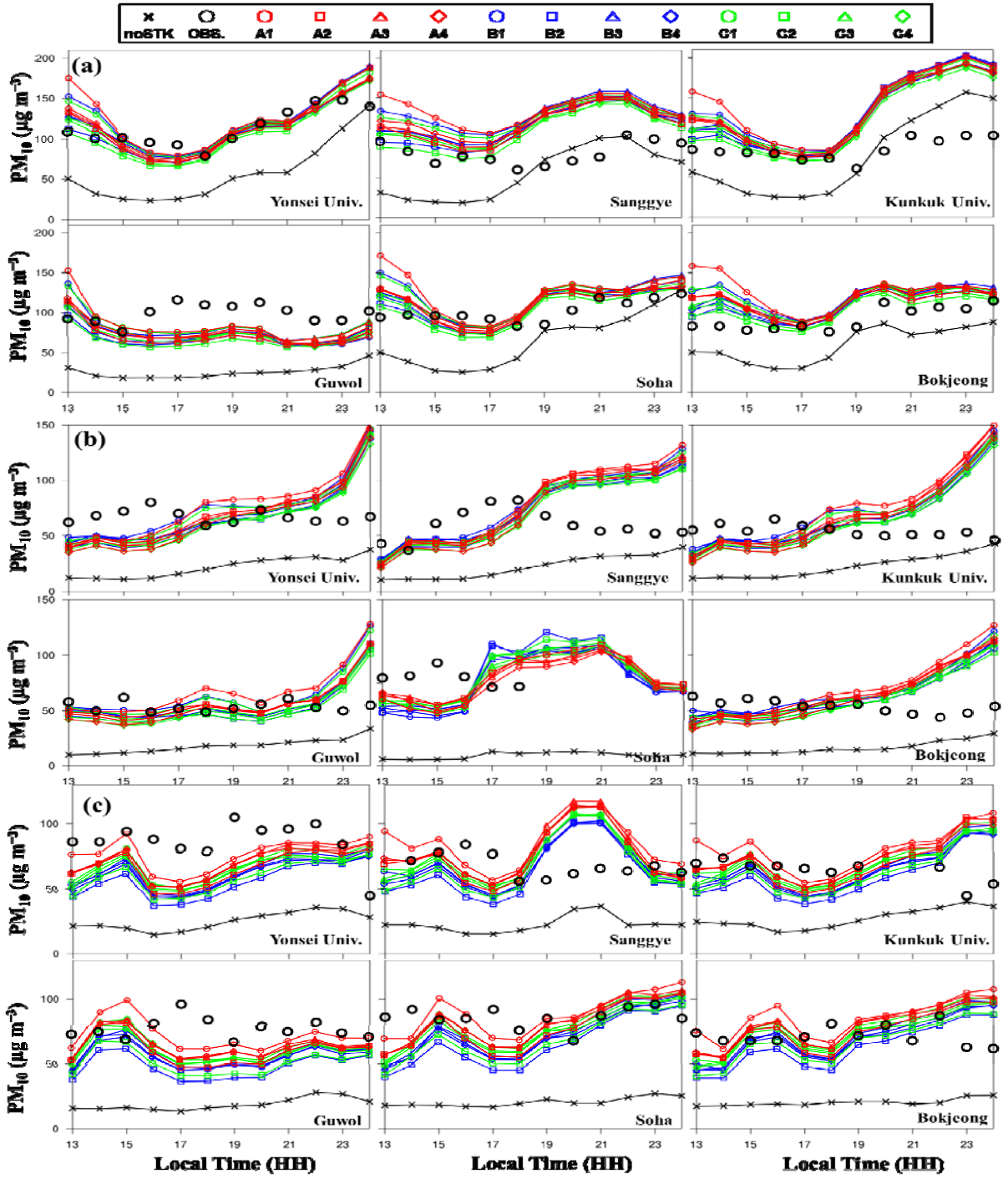


Figure 7. Time series of hourly PM_{10} for the six sites over SMA for 9 April (a), for 6 May (b), and for 16 May (c) in 2012. Observed concentrations are shown as the black circle and the model outputs as the colored line with their own markers explained in the legend.

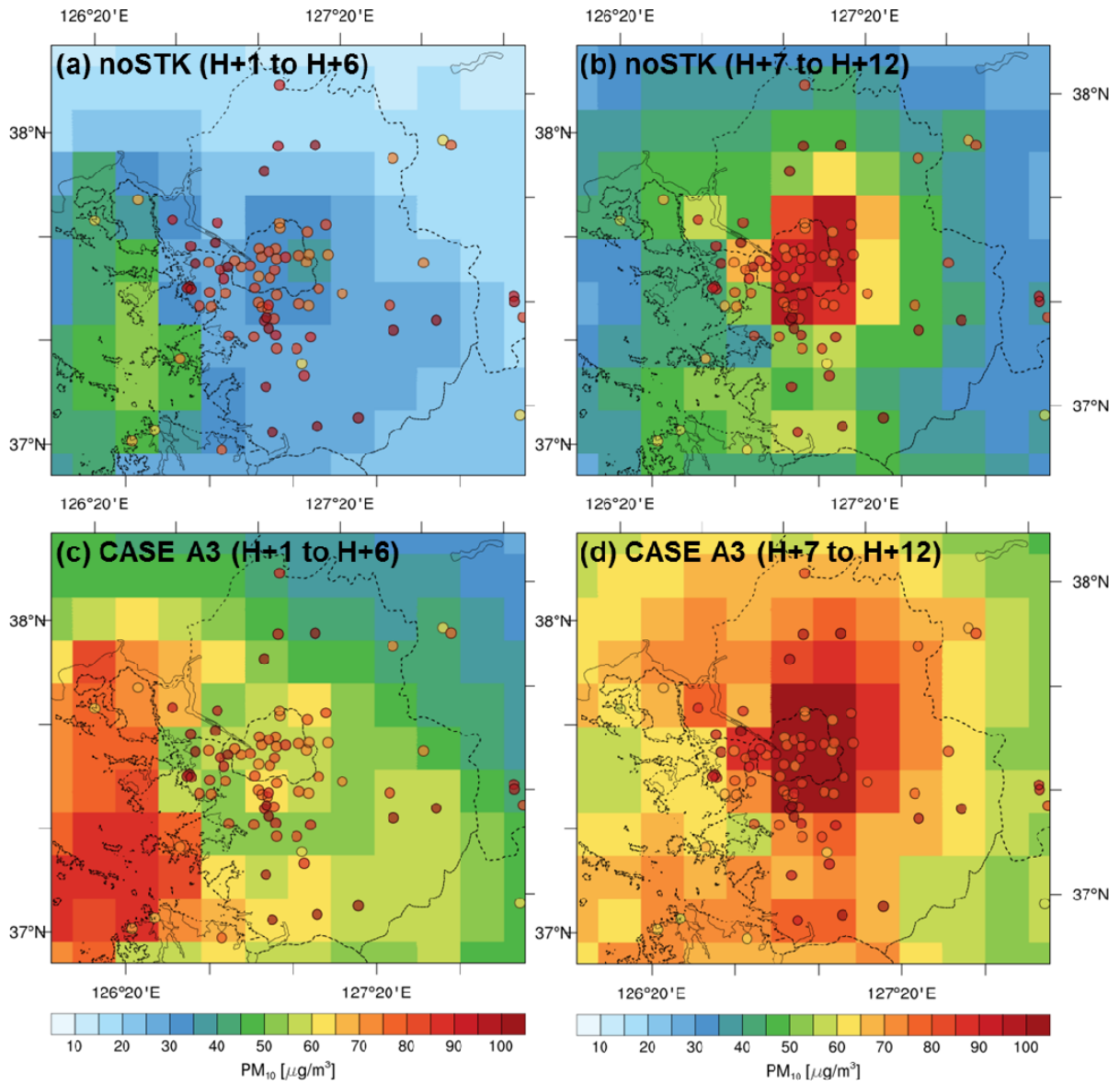


Figure 8. Averaged PM_{10} of noSTK case from H+1 to H+6 (a) and from H+7 to H+13 (b), and the averaged concentrations of case A3 at the same time series ((c) and (d)) for the selected ten days. Averaged NAMIS PM_{10} observations are shown with colored circles.

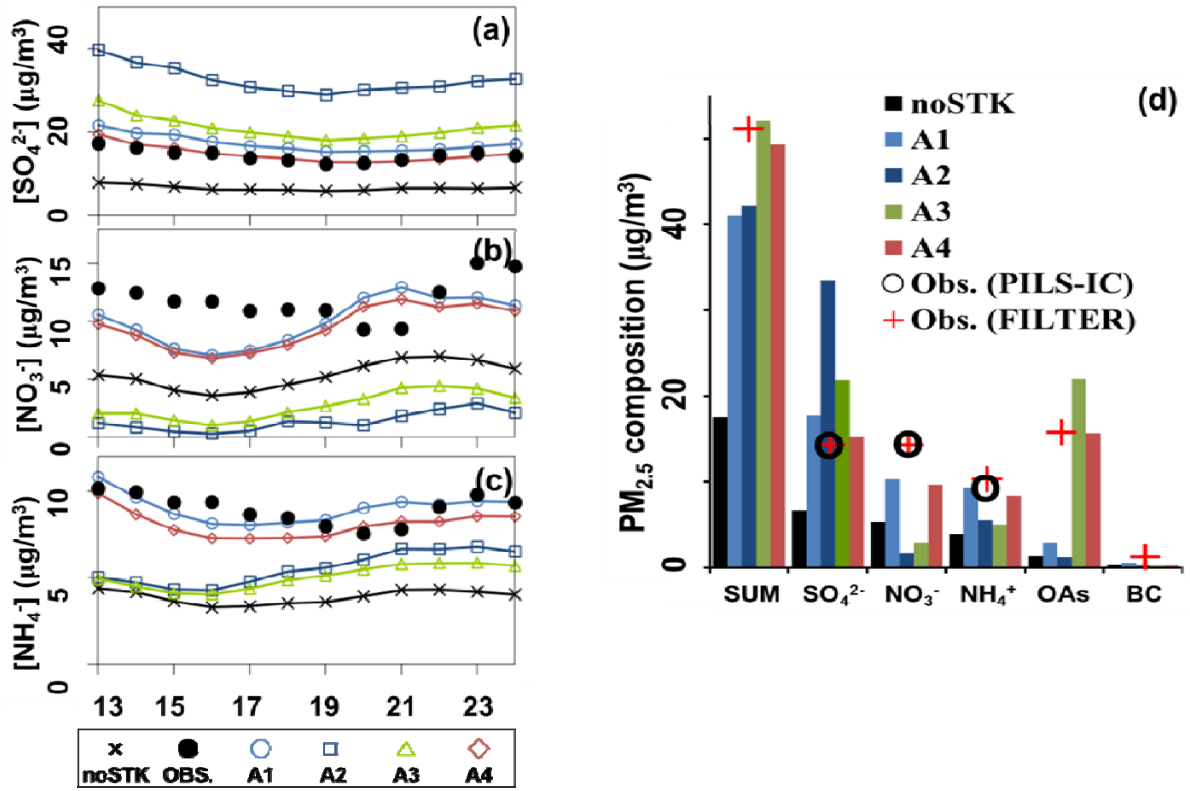


Figure 9. Time-series comparison of 1-hr averaged (a) SO_4^{2-} , (b) NO_3^- , and (c) NH_4^+ concentrations measured from PILS-IC instrument and model-predicted concentrations. In panel (d), 24-h averaged aerosol concentration in $\text{PM}_{2.5}$ from observations (PILS-IC instrument and low air volume sampler with Teflon filter) are compared with hindcast concentrations at the Yongin City site for ten selected episodes.

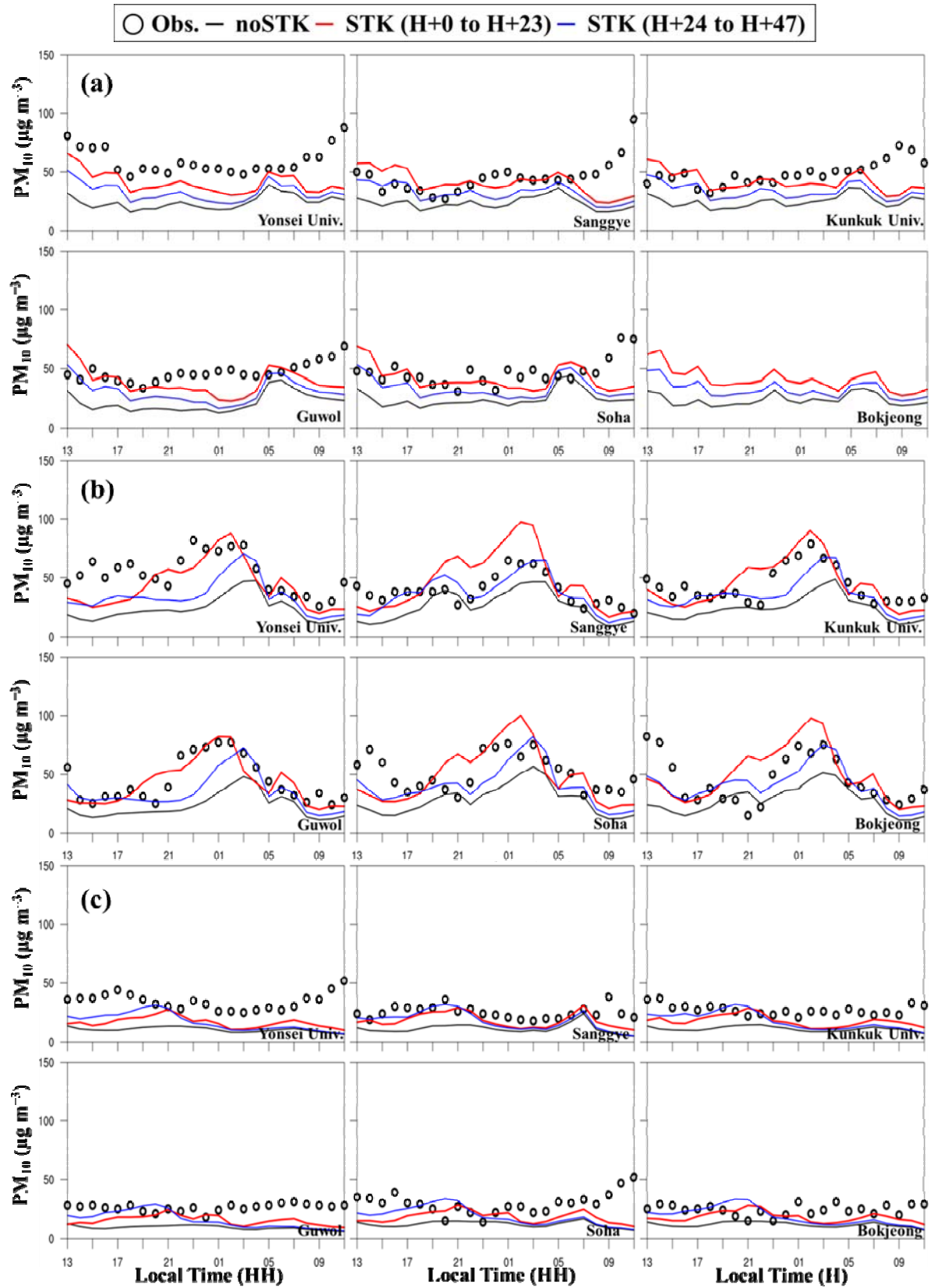


Figure 10. Time series of hourly PM_{10} at six sites in SMA for 8 March (a), for 10 March (b), and for 11 March (c) in 2012. Observed concentrations are denoted as black circles and the modelled concentrations are as colored lines.

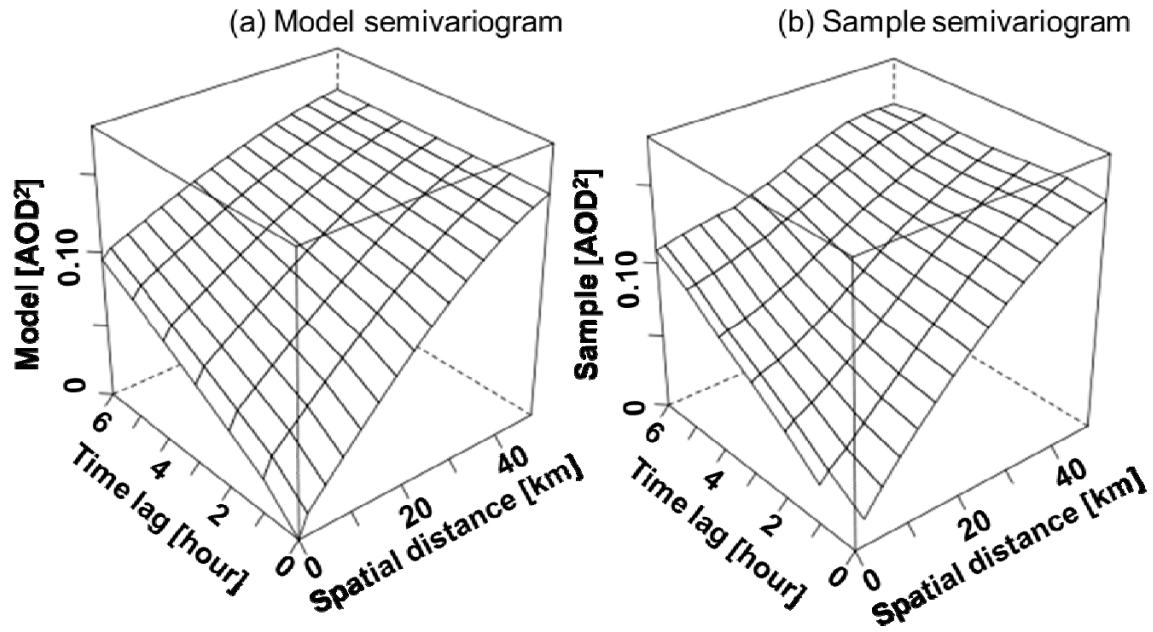


Figure A1. Daily three-dimensional semivariogram from fitted by the spherical model (a), and a sample semivariogram from the GOCI AOD data (b) on 8 April, 2012.

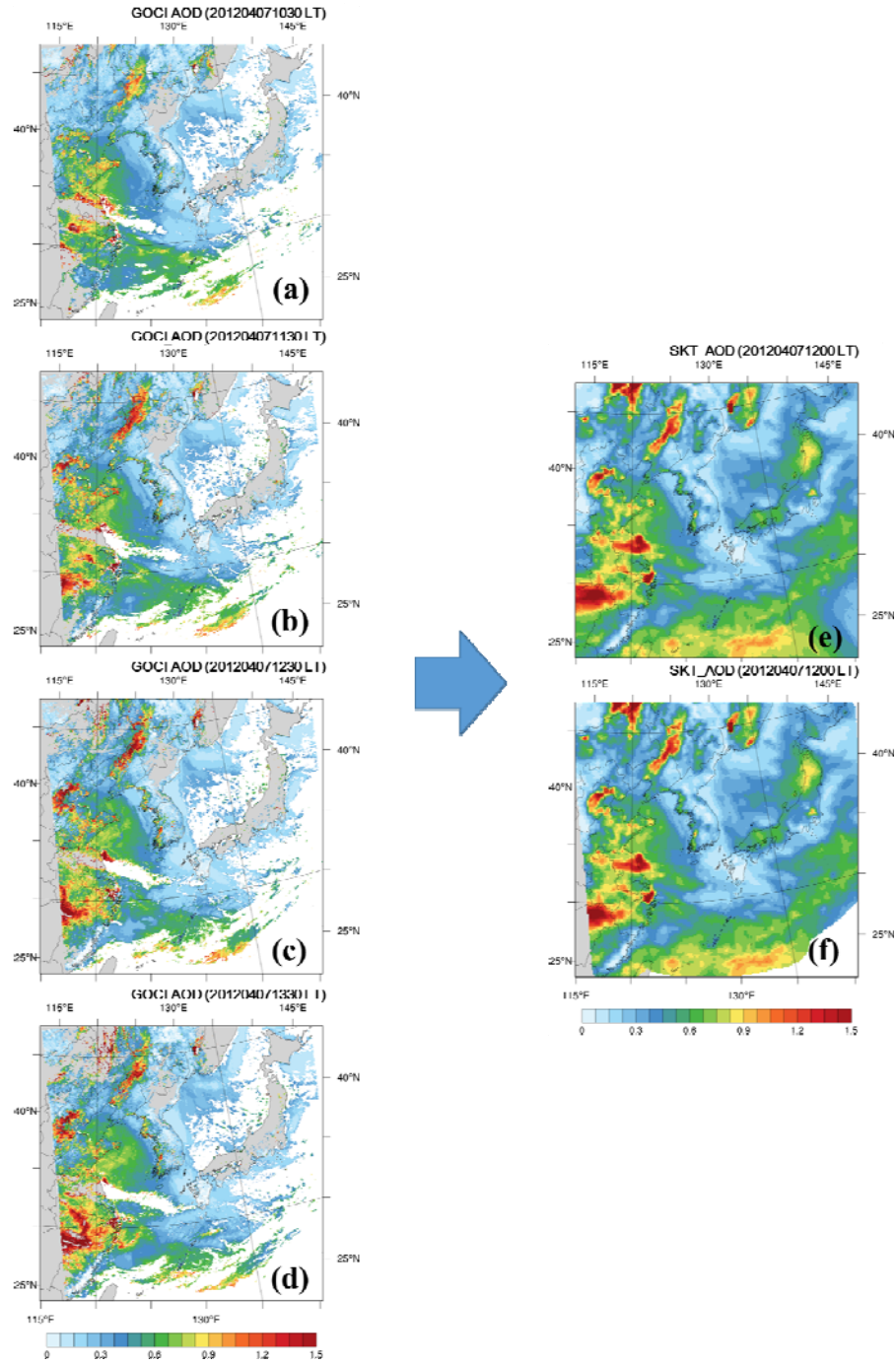


Figure A2. Spatial distributions of GOCI AOD from 10:30 to 13:30 LT ((a) to (d)) and ST-kriging AOD at 12:00 LT (e) on 7 April, 2012. The ST-kriging AOD at 12:00 LT with a criteria of kriging variances (KVs) less than 0.04 is also shown in (f).